



Cite this: *Nanoscale Adv.*, 2023, **5**, 4735

## Synergistic redox enhancement: silver phosphate augmentation for optimizing magnesium copper phosphate in efficient energy storage devices and oxygen evolution reaction<sup>†</sup>

Haseebul Hassan,<sup>a</sup> Muhammad Waqas Iqbal,<sup>ID \*a</sup> Nora Hamad Al-Shaalan,<sup>ID b</sup> Sarah Alharthi,<sup>ID c</sup> Nawal D. Alqarni,<sup>d</sup> Mohammed A. Amin<sup>c</sup> and Amir Muhammad Afzal<sup>a</sup>

The implementation of battery-like electrode materials with complicated hollow structures, large surface areas, and excellent redox properties is an attractive strategy to improve the performance of hybrid supercapacitors. The efficiency of a supercapattery is determined by its energy density, rate capabilities, and electrode reliability. In this study, a magnesium copper phosphate nanocomposite ( $MgCuPO_4$ ) was synthesized using a hydrothermal technique, and silver phosphate ( $Ag_3PO_4$ ) was decorated on its surface using a sonochemical technique. Morphological analyses demonstrated that  $Ag_3PO_4$  was closely bound to the surface of amorphous  $MgCuPO_4$ . The  $MgCuPO_4$  nanocomposite electrode showed a  $1138\text{ C g}^{-1}$  capacity at  $2\text{ A g}^{-1}$  with considerably improved capacity retention of 59% at  $3.2\text{ A g}^{-1}$ . The increased capacity retention was due to the fast movement of electrons and the presence of an excess of active sites for the diffusion of ions from the porous  $Ag_3PO_4$  surface. The  $MgCuPO_4$ – $Ag_3PO_4$ //AC supercapattery showed  $49.4\text{ W h kg}^{-1}$  energy density at  $550\text{ W kg}^{-1}$  power density and outstanding capacity retention (92% after 5000 cycles). The experimental findings for the oxygen evolution reaction reveal that the initial increase in potential required for  $MgCuPO_4$ – $Ag_3PO_4$  is 142 mV, indicating a clear Tafel slope of  $49\text{ mV dec}^{-1}$ .

Received 28th June 2023

Accepted 4th August 2023

DOI: 10.1039/d3na00466j

rsc.li/nanoscale-advances

### 1. Introduction

Nowadays, the most commonly used energy resources are fossil fuels, which lead to the emission of hazardous gases into the environment. Moreover, the increasing demand for energy is resulting in the quick depletion of these energy resources. All of these circumstances require renewable energy resources to fulfill energy requirements. However, due to the intermittent behavior of wind and solar energy resources, the use of energy storage devices (ESDs) has become more prominent. An ESD balances the demands and supply of electricity. Two similar kinds of electrode are used in electric double-layer capacitors (EDLCs) that deliver quick bursts of energy, long cycle life, and

exceptional power density. However, they have low energy density, limiting their ability to meet increasing technological needs.<sup>1,2</sup> Lithium-ion batteries have high energy but have a disadvantage in delivering quick bursts of energy, which significantly lowers their life span compared to an EDLC. Furthermore, if overloaded or overheated, an LIB can explode.<sup>3,4</sup> There have been numerous efforts to broaden the EDLC working potential and increase its energy while maintaining its power density. A new asymmetric device known as a supercapattery has recently received a lot of attention because it combines capacitive-graded materials (electrostatic storage) and other battery-graded materials (faradaic storage).  $RuO_2$ , a well-known outstanding pseudocapacitor electrode, demonstrated an exceptional capacitance of  $1340\text{ F g}^{-1}$ . But its high expense and ecotoxicity prevent it from being used commercially. Other oxide-based metals, such as  $NiO$  and  $Co_3O_4$ , show promise, but their electrical resistance is low. As a result, it is critical to identify materials for a supercapattery that are inexpensive but have similar effectiveness to current materials.<sup>5,6</sup> The catalysts used in the oxygen electrode for the oxygen evolution reaction (OER) have garnered significant attention due to their crucial role in these systems. There is an urgent need to develop highly efficient catalysts, free of noble metals,

<sup>a</sup>Department of Physics, Riphah International University, Campus Lahore, Pakistan.  
E-mail: waqas.iqbal@riphah.edu.pk

<sup>b</sup>Department of Chemistry, College of Science, Princess Nourah Bint Abdulrahman University, P. O. Box 84428, Riyadh 11671, Saudi Arabia

<sup>c</sup>Department of Chemistry, College of Science, Taif University, P. O. Box 11099, Taif, Saudi Arabia

<sup>d</sup>Department of Chemistry, College of Science, University of Bisha, Bisha, 61922, Saudi Arabia

<sup>†</sup> Electronic supplementary information (ESI) available. See DOI: <https://doi.org/10.1039/d3na00466j>



that exhibit superior catalytic activity for the OER. This need arises from the desire to replace expensive and scarce RuO<sub>2</sub> and IrO<sub>2</sub> catalysts.<sup>7</sup>

Scientists are presently focusing on tertiary phosphides as encouraging electrodes in supercapacitors. For example, Lei *et al.*<sup>8</sup> used a simple hydrothermal process to make a ZnNiCoP-NF nanostructure, which showed 1111 C g<sup>-1</sup> capacity at 10 A g<sup>-1</sup>. They demonstrated that the fabricated electrochemical design is ideal for energy-storage uses. Yang *et al.*<sup>9</sup> produced Ni-Co-Mo ternary phosphide formed on carbon cloth fibers, which had a specific capacitance of 433 F g<sup>-1</sup> at 1 A g<sup>-1</sup> current density.

Silver is undoubtedly a viable substitute for carbon-based materials. Moon *et al.*<sup>10</sup> developed a translucent and flexible supercapacitor with silver nanowires coated with gold. Despite their widespread use in bendable and wearable electrical devices, silver nanowire networks have high contact resistance among the nanowires.<sup>11-13</sup> Silver nanoparticles with graphene, metal oxides, carbon nanotubes, and conducting polymers were tried earlier. A matrix of Ag with carbon in a composite form shows no pseudocapacitance. However, due to the increased electrical activity, its EDLC performance improves. The Ag/PANI nanocomposite synthesized by Patil *et al.*<sup>14</sup> and Tang *et al.*<sup>15</sup> showed that the presence of Ag in a PANI heterostructure makes the movement of ions faster. The Ag coating on PANI produces high specific energy due to quicker electron transport and electrolyte access *via* a porous network.<sup>16</sup> Copper phosphate (Cu<sub>2</sub>PO<sub>4</sub>) is thought to be a perfect alternative to conventional metallic phosphates since Cu has significantly greater conductance. Cu<sub>2</sub>PO<sub>4</sub> exhibits further intriguing dielectric and thermal characteristics. The efficacy of Cu<sub>2</sub>PO<sub>4</sub> in supercapacitors has received little attention. Its electrochemical performance was improved by incorporating metal ions, which increases the conductivity. Thus, additional attempts to enhance the electrical conductivity of such electrode materials are required. The addition of another metal ion with similar properties can significantly improve the electrical characteristics. Thus, the movement of ions between the two metal phosphates becomes easier and the interfacial impedance of the composite substance can be reduced. Additionally, a large useful surface area is accessible for a redox reaction, increasing the capacity and power density of the supercapacitor.<sup>17</sup>

Herein, precipitation followed by calcination was used to produce silver phosphate nanoparticles (Ag<sub>3</sub>PO<sub>4</sub> NPs) on amorphous MgCuPO<sub>4</sub>. Because of its high electrical conductivity, Ag was selected to improve the electrical conductivity of amorphous MgCuPO<sub>4</sub>. To prevent the recombination of particles, an amorphous MgCuPO<sub>4</sub> and silver complex (Ag(NH<sub>3</sub>)<sub>2</sub><sup>+</sup>) mixture was made using a sonochemical technique. MgCuPO<sub>4</sub>-Ag<sub>3</sub>PO<sub>4</sub> composites were developed to raise the energy density, reduce resistance, and expand the supercapattery cycle life. The presence of low- $E_g$  metal ions in the amorphous structure of MgCuPO<sub>4</sub> is still a novel way to increase the supercapacitive performance. Furthermore, the application of the oxygen evolution reaction (OER) was also examined in the context of MgCuPO<sub>4</sub>-Ag<sub>3</sub>PO<sub>4</sub> composites. The impact of different MgCuPO<sub>4</sub> to Ag<sub>3</sub>PO<sub>4</sub> weight ratios on the overall storage

capability was investigated. A comprehensive charge transfer procedure between MgCuPO<sub>4</sub> and solid Ag<sub>3</sub>PO<sub>4</sub> was observed.

## 2. Experimental work

### 2.1. Materials

Carbon black, magnesium nitrate hexahydrate (Mg(NO<sub>3</sub>)<sub>2</sub>·6H<sub>2</sub>O), hydrochloric acid (HCl), copper(II) nitrate tri-hydrate (Cu(NO<sub>3</sub>)<sub>2</sub>·3H<sub>2</sub>O), NMP, and silver nitrate (AgNO<sub>3</sub>) were received from Friendemann Schmidt. Tri-sodium phosphate (Na<sub>3</sub>PO<sub>4</sub>) and potassium hydroxide pellets (KOH) were bought from Duksan Pure Chemicals. All of the materials used were of analytical quality and were used without purification. Deionized water (DIW) was used throughout the experiments.

### 2.2. Synthesis of MgCuPO<sub>4</sub>-Ag<sub>3</sub>PO<sub>4</sub>

A hydrothermal and sonochemical technique was used to synthesize MgCuPO<sub>4</sub>-Ag<sub>3</sub>PO<sub>4</sub> composites with various weight ratios of MgCuPO<sub>4</sub> and Ag<sub>3</sub>PO<sub>4</sub>. The as-prepared MgCuPO<sub>4</sub> (set A) was made using the methods described in the literature.<sup>18</sup> First, 0.8 M magnesium nitrate hexahydrate (Mg(NO<sub>3</sub>)<sub>2</sub>·6H<sub>2</sub>O) solution was mixed with a 0.8 M solution of copper(II) nitrate tri-hydrate (Cu(NO<sub>3</sub>)<sub>2</sub>·3H<sub>2</sub>O). The mixture was stirred continuously for 25 min and transferred into an autoclave and heated at 140 °C. The centrifuge machine (10 000 rpm Model RST-10M) was used to eliminate impurities from the solution. After drying at 40 °C the prepared MgCuPO<sub>4</sub> was collected. The addition of NH<sub>3</sub> into a 0.5 M solution of AgNO<sub>3</sub> reduces Ag<sup>+</sup>. A horn sonicator was used for sonication until a diaminesilver(I) complex was produced. The complex solution of diaminesilver(I) was then combined with 0.02 g of MgCuPO<sub>4</sub> solution and continuously stirred (3–4 h). The mixture was rinsed many times with DIW before drying for 4 h at 40 °C. Finally, the desiccated materials were calcined for 3 h at 300 °C and labeled S<sub>1</sub>. Two more MgCuPO<sub>4</sub>-Ag<sub>3</sub>PO<sub>4</sub> nanocomposites were made for optimization reasons by altering the wt% ratio of as-prepared MgCuPO<sub>4</sub> to 0.03 and 0.05 g and they were designated S<sub>2</sub> and S<sub>3</sub>, respectively. Fig. 1 shows the synthetic process for MgCuPO<sub>4</sub>-Ag<sub>3</sub>PO<sub>4</sub> nanocomposites. Table 1 shows different wt% ratios in three different composites of MgCuPO<sub>4</sub>-Ag<sub>3</sub>PO<sub>4</sub> (S<sub>1</sub>, S<sub>2</sub>, and S<sub>3</sub>).

### 2.3. Characterization

**2.3.1. Structural and surface analysis.** The crystalline phases of the materials (MgCuPO<sub>4</sub>, S<sub>1</sub>, S<sub>2</sub>, and S<sub>3</sub>) were analyzed using XRD (D5000, Siemens). K $\alpha$  radiation with 1.54 Å wavelength and 0.02 s<sup>-1</sup> scan rate was used to determine the crystallinity of S<sub>1</sub>, S<sub>2</sub>, and S<sub>3</sub>. FTIR (Thermo Scientific Nicolet IS10 Smart ITR) was used to investigate the purity of the samples (S<sub>1</sub>, S<sub>2</sub>, and S<sub>3</sub>) which were scanned at 1 cm<sup>-1</sup> resolution. X-ray photoelectron spectroscopy (XPS) measurements were taken at binding energies from 0 to 1000 eV, with 1 eV resolution. Single XPS spectra were performed at a resolution of 0.1 eV. Origin Pro 8.1 was used to fit the spectra with numerous Gaussian curves. Scanning electron microscopy (SEM) was applied to analyze the morphological characteristics of the MgCuPO<sub>4</sub>-Ag<sub>3</sub>PO<sub>4</sub>

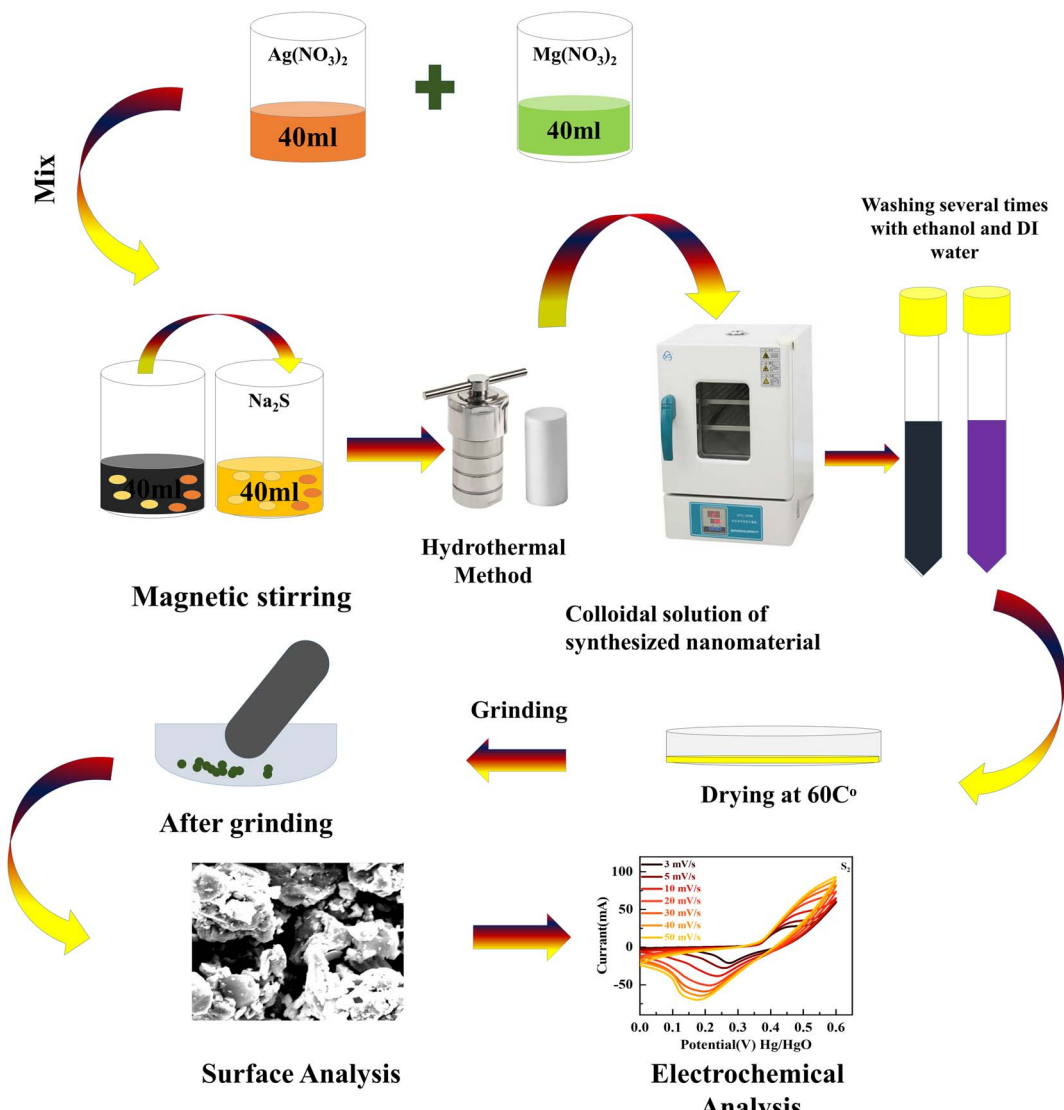


Fig. 1 Systematic illustration of the hydrothermal technique to synthesize  $\text{MgCuPO}_4\text{--Ag}_3\text{PO}_4$  nanocomposites.

Table 1 Different weight ratios of Ag to  $\text{MgCuPO}_4$  for the synthesis of  $\text{MgCuPO}_4\text{--Ag}_3\text{PO}_4$  nanocomposites

Sample	$\text{MgCuPO}_4$ mass	Ag mass	Weight ratio (%)
$S_1$	20 mg	0.4 mg	0.083 : 1
$S_2$	30 mg	0.4 mg	0.145 : 1
$S_3$	50 mg	0.4 mg	0.232 : 1

nanocomposites. Jenway's 6800 design was used to determine the optical absorbance characteristics over a spectral range of 200 to 800 nm.

**2.3.2. Electrochemical studies.** The active materials ( $S_1$ ,  $S_2$ , and  $S_3$ ) were coated onto nickel foam (NF) and employed as a working electrode in an electrochemical research setup. In a three-cell setup, the counter and reference electrodes were platinum wire and  $\text{Hg}/\text{HgO}$ , respectively. Throughout the

electrochemical studies in a typical cell, a 1 M potassium hydroxide (KOH) solution was kept constant. The slurry for the working electrode was prepared by blending 75% active material ( $\text{MgCuPO}_4\text{--Ag}_3\text{PO}_4$ ) and 15% carbon black, which were bonded together with the help of PVDF binder (10%). This slurry was mixed continuously for 5–6 h to produce a homogeneous suspension. This suspension was then easily applied to NF. Before starting the experiment, the NF was thoroughly cleaned with HCl, ethanol, acetone, and DIW. The NMP slurry was coated on a  $1 \times 1 \text{ cm}^2$  area of NF. The total weight of the active material was roughly 5.5 mg. Furthermore, in the supercapattery application, activated carbon (AC) and the best composite were used as the positive and negative electrodes. The electrochemical properties of all of the materials were studied using a workstation CS300 potentiostat. A multi-channel Autolab, PGSTAT30 potentiostat was used for the Mott–Schottky (MS) measurements.

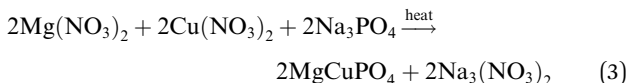
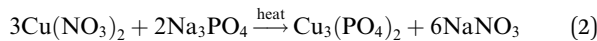
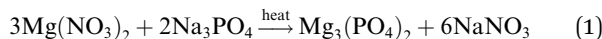


### 3. Results and discussion

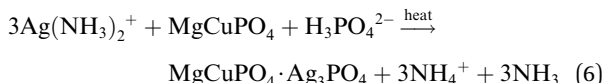
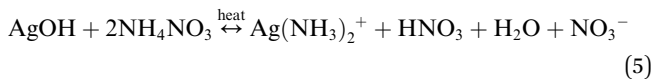
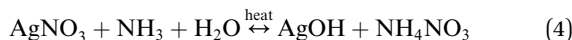
#### 3.1. Characterization of materials

**3.1.1. Mechanism of  $\text{MgCuPO}_4\text{-Ag}_3\text{PO}_4$  composite formation.** The equations below were used to describe the formation mechanism of the  $\text{MgCuPO}_4\text{-Ag}_3\text{PO}_4$  nanocomposite. In the first part, a homogeneous suspension of  $\text{MgCuPO}_4$  nanocomposite was formed using a hydrothermal approach. After that positive  $\text{Ag}(\text{NH}_3)_2^+$  was electrostatically bound with the phosphate group and arranged around  $\text{MgCuPO}_4$ . The presence of an excess amount of  $\text{H}_3\text{PO}_4^{2-}$  in the as-synthesized  $\text{MgCuPO}_4$  causes the quick development of a homogeneous  $\text{MgCuPO}_4\text{-Ag}_3\text{PO}_4$  nanocomposite after stirring. Ammonium ( $\text{NH}_4^+$ ) and other unwanted impurities were eliminated upon calcination.

$\text{MgCuPO}_4$  formation



$\text{MgCuPO}_4\text{-Ag}_3\text{PO}_4$  formation



**3.1.2. Structural analysis of  $\text{MgCuPO}_4\text{-AgPO}_4$ .** The crystallinities of  $\text{MgCuPO}_4$ ,  $\text{S}_1$ ,  $\text{S}_2$ , and  $\text{S}_3$  were studied by XRD and the outputs are depicted in Fig. 2. First, the XRD of  $\text{MgCuPO}_4$  was studied, as indicated by Fig. 2(a). There were three different XRD patterns represented by three different colors assigned to  $\text{Mg}_3(\text{PO}_4)_2$ ,  $\text{Cu}_3(\text{PO}_4)_2$ , and  $\text{MgCuPO}_4$ . The diffraction spikes at  $2\theta = 12^\circ, 22^\circ, 23.2^\circ, 26^\circ, 28.32^\circ, 31.3^\circ, 36.5^\circ, 38^\circ, 48.23^\circ, 52.8^\circ$ , and  $57.1^\circ$  belong to the  $(110)$ ,  $(101)$ ,  $(-111)$ ,  $(210)$ ,  $(021)$ ,  $(121)$ ,  $(-221)$ ,  $(031)$ ,  $(330)$ ,  $(-331)$ , and  $(150)$  planes, which match JCPDS 33-0876.<sup>19</sup> The XRD peaks for  $\text{Cu}_3(\text{PO}_4)_2$  showed diffraction spikes at  $2\theta = 15.32^\circ, 21.2^\circ, 25^\circ, 31.33^\circ, 35^\circ, 37^\circ, 40^\circ, 44.3^\circ$ , and  $56.5^\circ$  belonging to  $(001)$ ,  $(110)$ ,  $(-101)$ ,  $(001)$ ,  $(121)$ ,  $(210)$ ,  $(200)$ ,  $(013)$ , and  $(-221)$ , which matches JCPDS 01-080-0991.<sup>20</sup> The XRD pattern for  $\text{MgCuPO}_4$  indicated almost similar diffraction patterns to  $\text{Mg}_3(\text{PO}_4)_2$  and  $\text{Cu}_3(\text{PO}_4)_2$ . The width of these spikes was evidence of the amorphous nature of  $\text{MgCuPO}_4$ . The incorporation of  $\text{Ag}_3\text{PO}_4$  is indicated in Fig. 2(b). Three different XRD patterns for  $\text{S}_1$ ,  $\text{S}_2$ , and  $\text{S}_3$  are represented in Fig. 2(b). There were multiple reflections associated with  $\text{S}_1$ ,  $\text{S}_2$ , and  $\text{S}_3$ . The XRD pattern shows the crystalline nature of  $\text{Ag}_3\text{PO}_4$ . The strong peaks for  $\text{Ag}_3\text{PO}_4$  at  $2\theta = 29.1^\circ, 33.3^\circ, 36.6^\circ$ ,

$47.5^\circ, 52.1^\circ, 55.0^\circ$ , and  $57.5^\circ$  correspond to the  $(200)$ ,  $(210)$ ,  $(211)$ ,  $(310)$ ,  $(222)$ ,  $(320)$ , and  $(321)$  planes. This XRD pattern correlated with JCPDS 06-0505, which shows the formation of  $\text{Ag}_3\text{PO}_4$ .<sup>21</sup> As the amount of  $\text{MgCuPO}_4$  decreased, the intensity of XRD spikes for  $\text{Ag}_3\text{PO}_4$  increased. The lack of a positional shift in the  $\text{Ag}_3\text{PO}_4$  peaks indicates that  $\text{Ag}_3\text{PO}_4$  was not incorporated into the  $\text{MgCuPO}_4$  lattice, but rather developed on the  $\text{MgCuPO}_4$  surface.<sup>22</sup> Table 2 shows the lattice parameters of the samples.

The specific surface areas (SSAs) of  $\text{MgCuPO}_4$  and the  $\text{MgCuPO}_4\text{-Ag}_3\text{PO}_4$  ( $\text{S}_2$ ) nanocomposite were calculated using the Brunauer–Emmett–Teller (BET) technique, because  $\text{S}_2$  demonstrated the best performance compared to  $\text{S}_1$  and  $\text{S}_3$ , as described in the following part. The  $\text{N}_2$  adsorption–desorption isotherms of  $\text{MgCuPO}_4$  and  $\text{S}_2$  are shown in Fig. 2(c) and (d). The BET graphs for  $\text{MgCuPO}_4$  and  $\text{S}_2$  exhibit an IV-type hysteresis loop, showing their porous structure. The porous behavior of  $\text{MgCuPO}_4$  and  $\text{S}_2$  resulted in decreases in electrolyte ion diffusion time. The SSA of  $\text{MgCuPO}_4$  and  $\text{S}_2$  were  $15.72$  and  $19.34 \text{ m}^2 \text{ g}^{-1}$ , respectively. The total pore volumes for  $\text{MgCuPO}_4$  and  $\text{S}_2$  estimated through BET calculations were  $0.04928$  and  $0.052596 \text{ cm}^3 \text{ g}^{-1}$ , respectively. The smaller SSA and pore volume of  $\text{MgCuPO}_4$  compared to  $\text{S}_2$  were due to the absence of  $\text{Ag}_3\text{PO}_4$  in the  $\text{MgCuPO}_4\text{-Ag}_3\text{PO}_4$  nanocomposite. Furthermore, this may be due to the distribution of  $\text{Ag}_3\text{PO}_4$  NPs into  $\text{MgCuPO}_4$ .<sup>23</sup>

Fig. 3(a) and (b) show the FTIR spectra of amorphous  $\text{MgCuPO}_4$ ,  $\text{S}_1$ ,  $\text{S}_2$ , and  $\text{S}_3$ . The band for the O–P–O bond ( $\nu_4 \text{ PO}_4^{3-}$ ) for the triply degenerate asymmetric mode occurred at  $563 \text{ cm}^{-1}$ . While the band at  $1036 \text{ cm}^{-1}$  belongs to the P–O bond ( $\nu_3 \text{ PO}_4^{3-}$ ) stretching mode. The above-mentioned bands are evidence of the presence of phosphate ( $\text{PO}_4^{3-}$ ). The bands moved to a lower wavenumber as the amount of  $\text{Ag}_3\text{PO}_4$  increased in the  $\text{MgCuPO}_4\text{-Ag}_3\text{PO}_4$  nanocomposites.<sup>24</sup> The band appearing at  $1645 \text{ cm}^{-1}$  belongs to  $\nu_1 (\text{A}_1) \text{ H}_2\text{O}$  and those at  $3200\text{--}3800 \text{ cm}^{-1}$  belong to  $\nu_2 (\text{A}_1) \text{ H}_2\text{O}$ . After the incorporation of  $\text{Ag}_3\text{PO}_4$  ( $\text{S}_1$ ,  $\text{S}_2$ , and  $\text{S}_3$ ), the band intensities rose considerably, showing that the percentages of phosphorous and water on the  $\text{MgCuPO}_4\text{-Ag}_3\text{PO}_4$  surface increased.<sup>25</sup> The adsorbed water resulted in increased storage performance due to an enhanced inter-particle path.<sup>26,27</sup>

**3.1.3. Optical properties of  $\text{MgCuPO}_4\text{-AgPO}_4$ .** UV-vis absorption spectroscopy was applied to check the impact of  $\text{Ag}_3\text{PO}_4$  on the optical performance of  $\text{MgCuPO}_4$ . The spectra are shown in Fig. 3(c). In a deformed octahedral coordinated environment,  $\text{MgCuPO}_4$  has an absorption edge at  $808 \text{ nm}$  and a second absorption edge at  $1000 \text{ nm}$ , which are due to  $\text{Cu}^+$  and  $\text{Mg}^+$ , respectively.<sup>28,29</sup> Because of the decreasing fractions of  $\text{MgCuPO}_4$  found in  $\text{MgCuPO}_4\text{-Ag}_3\text{PO}_4$  nanocomposites, the absorptivity of  $\text{MgCuPO}_4$  progressively declines from  $\text{S}_1$  to  $\text{S}_3$ . Furthermore, as the proportions of  $\text{MgCuPO}_4$  decreased, the absorption edge red shifted towards the visible region. The existence of more  $\text{Ag}_3\text{PO}_4$  NPs than  $\text{MgCuPO}_4$ , which absorbs in the visible region, causes the peaks to redshift. This redshift may also be due to narrowing of the band gap, as evidenced by the altered Kubelka–Munk function of light energy ( $\alpha h\nu$ )<sup>2</sup> versus photon energy ( $h\nu$ ), as shown in Fig. 3(d). The Tauc equation



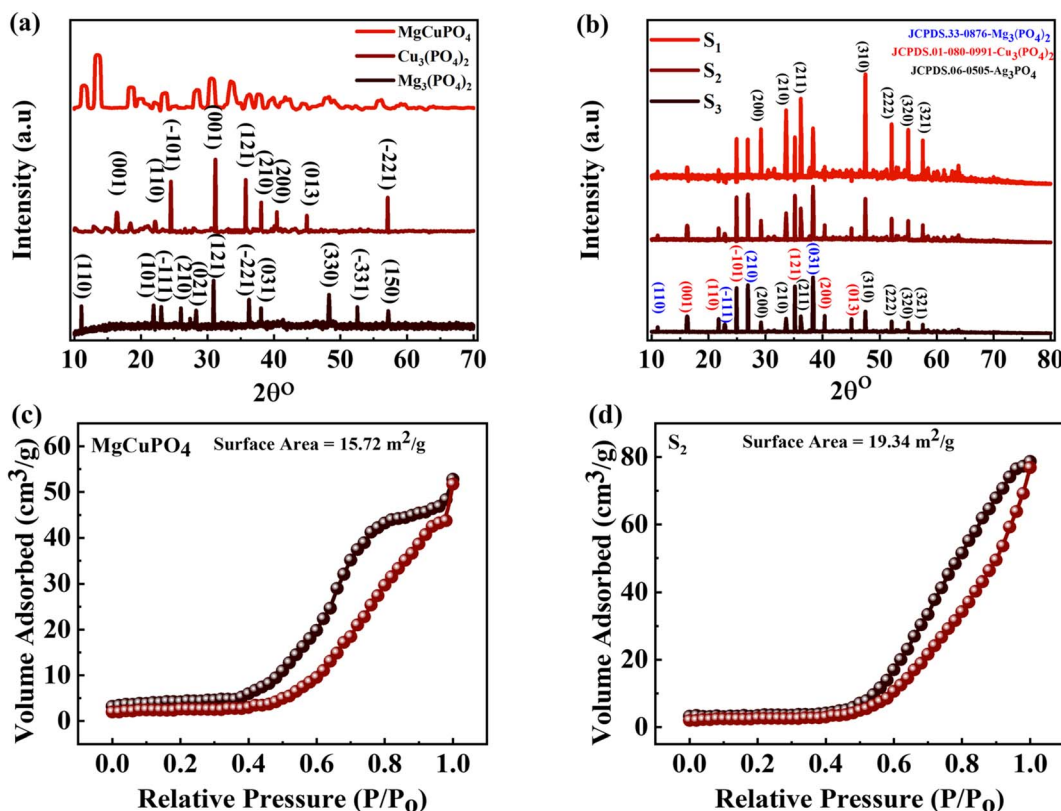


Fig. 2 (a) The XRD pattern for Mg<sub>3</sub>(PO<sub>4</sub>)<sub>2</sub>, Cu<sub>3</sub>(PO<sub>4</sub>)<sub>2</sub>, and MgCuPO<sub>4</sub>. (b) The XRD pattern for MgCuPO<sub>4</sub>-Ag<sub>3</sub>PO<sub>4</sub> (S<sub>1</sub>, S<sub>2</sub>, S<sub>3</sub>) nanocomposites. (c and d) BET measurement for MgCuPO<sub>4</sub> and the S<sub>2</sub> nanocomposite.

was used to determine the band gap ( $E_g$ ) values of the samples.<sup>30,31</sup>

$$(\alpha h\nu)^2 = K(h\nu - E_g) \quad (7)$$

The absorption coefficient is denoted by  $\alpha$  and the proportionality constant by  $K$ .  $K$  was determined from  $K = (2.303 \times 10^3)(A)/L$ , where absorbance is represented by  $A$  and optical path by  $L$  (1 cm). The  $E_g$  value was estimated by extrapolating the straight line of the image shown in Fig. 3(d).  $E_g$  values for S<sub>1</sub>, S<sub>2</sub>, and S<sub>3</sub> and amorphous MgCuPO<sub>4</sub> were 3.9, 3.6, 3.5, and 4.3 eV, respectively. The electrical insulating properties of amorphous MgCuPO<sub>4</sub> were reflected in its high  $E_g$  value. The gradual drop in  $E_g$  in MgCuPO<sub>4</sub>-AgPO<sub>4</sub> nanocomposites was due to the combined impact between the two elements. The overlapping of energy levels causes a reduction in the band gap according to

energy band theory. This indicates that Ag<sub>3</sub>PO<sub>4</sub> were well developed on the MgCuPO<sub>4</sub> surface, exhibiting the combined electronic characteristics.<sup>32,33</sup>

**3.1.4. XPS spectrum for MgCuPO<sub>4</sub>-AgPO<sub>4</sub>.** Because of the dispersion of Ag<sub>3</sub>PO<sub>4</sub> NPs on the MgCuPO<sub>4</sub> surface, XPS was used to analyze the surface composition of MgCuPO<sub>4</sub> and MgCuPO<sub>4</sub>-AgPO<sub>4</sub> nanocomposites. The XPS spectrum of S<sub>2</sub> showed the presence of several distinct peaks due to Mg, P, C 1s, Ag, O 1s, and Cu, as indicated in Fig. 4(a). Fig. 4(b) depicts the deconvoluted core level spectrum of Mg 2p, which includes two bands at 49 and 51 eV binding energy corresponding to Mg<sup>2+</sup> and Mg<sup>0</sup>, respectively.<sup>34</sup> The XPS spike for Cu 2p<sub>3/2</sub> located at 932.5 eV correlates to Cu<sup>2+</sup> possibly reacting with a phosphate ion. The peak for Cu 2p<sub>1/2</sub> appeared at 952.5 eV, as indicated in Fig. 4(c).<sup>35</sup> The XPS spectrum for P 2p is represented in Fig. 4(d).

Table 2 Structural parameters for the analysis of MgCuPO<sub>4</sub> and MgCuPO<sub>4</sub>-Ag<sub>3</sub>PO<sub>4</sub> nanocomposites

Sample	Lattice parameters			Volume (nm) <sup>3</sup>	Particle size (nm)	Strain ( $\varepsilon_r$ ) (10 <sup>-3</sup> )	Density (g cm <sup>-3</sup> )	Dislocation density (10 <sup>15</sup> m <sup>-2</sup> )
	$\alpha$	$\beta$	$\Gamma$					
Standard	7.599	8.235	5.076					
MgCuPO <sub>4</sub>	7.597	8.237	5.075	0.38	40–50	0.65	5.4087	0.55
S <sub>1</sub>	7.600	8.240	5.075	0.41	51–56	0.71	5.4093	0.58
S <sub>2</sub>	7.613	8.243	5.074	0.43	53–58	0.69	5.4098	0.63
S <sub>3</sub>	7.615	8.247	5.074	0.44	52–59	0.70	5.4100	0.71



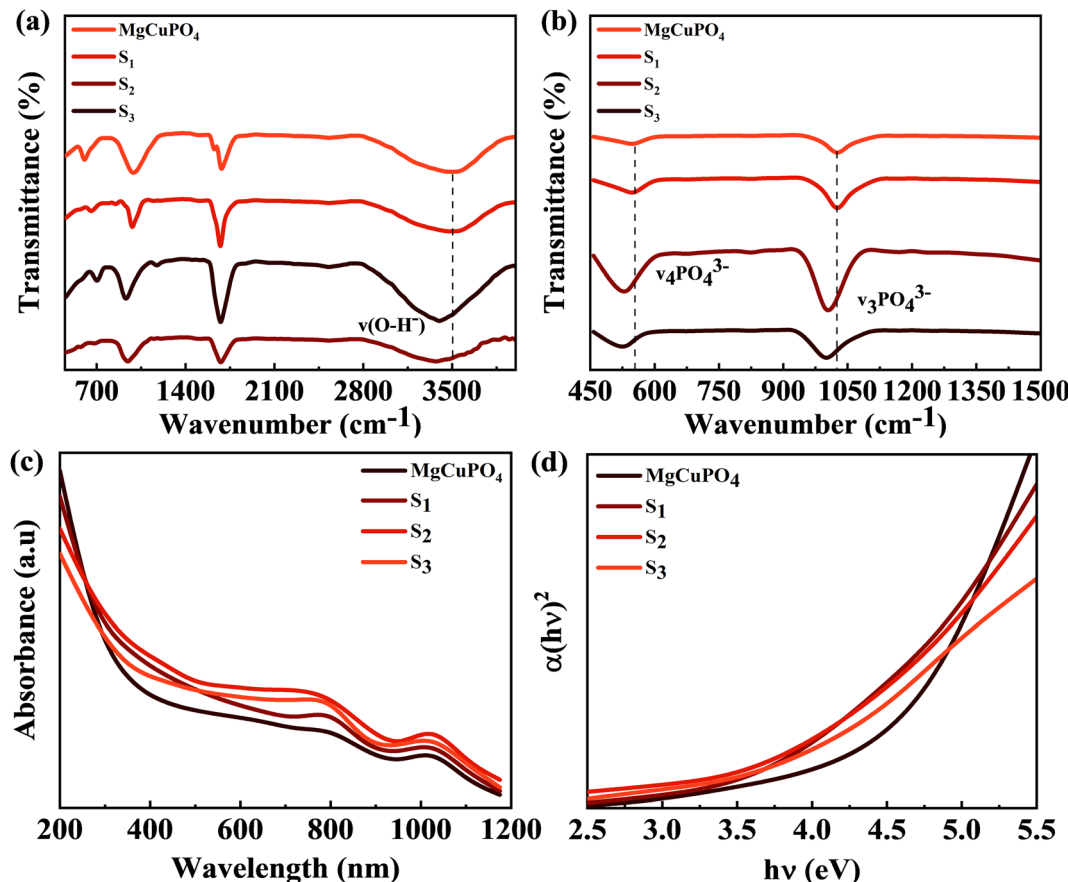


Fig. 3 (a) FTIR spectra for  $\text{MgCuPO}_4$ ,  $\text{S}_1$ ,  $\text{S}_2$ , and  $\text{S}_3$  at  $500\text{--}4000\text{ cm}^{-1}$ . (b) FTIR spectra for  $\text{MgCuPO}_4$ ,  $\text{S}_1$ ,  $\text{S}_2$ , and  $\text{S}_3$  at  $450\text{--}1500\text{ cm}^{-1}$ . (c) UV-vis spectra for  $\text{MgCuPO}_4$ ,  $\text{S}_1$ ,  $\text{S}_2$ , and  $\text{S}_3$ . (d) The band gap determination for  $\text{MgCuPO}_4$ ,  $\text{S}_1$ ,  $\text{S}_2$ , and  $\text{S}_3$ .

The presence of  $\text{P } 2\text{p}_{1/2}$  at 135 eV and  $\text{P } 2\text{p}_{3/2}$  at 133 eV confirm the presence of phosphorous. The deconvoluted XPS spectrum of  $\text{P } 2\text{p}$  showed that the first peak at 133 eV accounts for 75–80% of the  $\text{P } 2\text{p}$  signal. This can be ascribed to the oxidation of the  $\text{MgCuPO}_4$  surface metal phosphate molecule in  $\text{PO}_4^{3-}$ .<sup>36</sup> The second spike at 135 eV showed the presence of 10–20% residual metaphosphate.<sup>37</sup>  $\text{S}_2$  demonstrated the presence of symmetrical spin-orbit components. The XPS spectra for Ag showed two distinct peaks which were separated by 6 eV. The  $\text{Ag } 3\text{d}_{5/2}$  peak appeared at 368 eV and  $\text{Ag } 3\text{d}_{3/2}$  peak appeared at 374 eV, which corresponds to  $\text{Ag}^+$ , as indicated in Fig. 4(e).<sup>38</sup>

**3.1.5. Morphological study of  $\text{MgCuPO}_4\text{-AgPO}_4$ .** SEM analysis was used to examine the shape of  $\text{MgCuPO}_4$  and its three composites with  $\text{Ag}_3\text{PO}_4$  ( $\text{S}_1$ ,  $\text{S}_2$ , and  $\text{S}_3$ ). Fig. 5(a)–(d) depict an uneven form of amorphous  $\text{MgCuPO}_4$  and its composites with  $\text{Ag}_3\text{PO}_4$  with 40–50 nm particle size. Fig. 5 shows that as the amorphous  $\text{MgCuPO}_4$  content of the nanocomposite decreased, more  $\text{Ag}_3\text{PO}_4$  NPs were found on the surface of the amorphous  $\text{MgCuPO}_4$ . However, for  $\text{S}_1$  and  $\text{S}_3$ , the recombination of ions could restrict the diffusion of ions. The recombination of ions could be attributed to an overabundance of  $\text{Ag}_3\text{PO}_4$ , which restricts the movement of  $\text{MgCuPO}_4$  ions.<sup>39,40</sup>

### 3.2. Electrochemical results

The synthesized samples ( $\text{MgCuPO}_4$ ,  $\text{S}_1$ ,  $\text{S}_2$ , and  $\text{S}_3$ ) were then electrochemically tested using CV measurements, which were determined in the potential window (PW) of 0–0.6 V at a scan rate of  $3\text{--}50\text{ mV s}^{-1}$ , as depicted in Fig. 6. For all samples, faradaic behavior was observed from the presence of redox peaks. This was because of the faster movement of ions within the materials, causing a redox reaction at the surface of the electrodes.<sup>41,42</sup>  $\text{S}_2$  had the greatest redox current strength at  $3\text{ mV s}^{-1}$  scan rate compared to the other  $\text{MgCuPO}_4\text{-AgPO}_4$  nanocomposites. This shows that the addition of  $\text{Ag}_3\text{PO}_4$  increased the redox current due to the synergistic impact of  $\text{MgCuPO}_4$  and  $\text{Ag}_3\text{PO}_4$ . But further addition of  $\text{Ag}_3\text{PO}_4$  influenced the redox potentials, as can be seen from the CV plot of  $\text{S}_3$  (Fig. 6(d)). The finding suggested that electrolyte ions engage extensively with the numerous electro-active sites of the materials when the amount of  $\text{Ag}_3\text{PO}_4$  increases. With higher loadings of  $\text{Ag}_3\text{PO}_4$  in  $\text{MgCuPO}_4$ , the electrical transmission route and electrolyte ion diffusion rate of the nanocomposites differ. This indicated that the number of phosphate groups in the  $\text{MgCuPO}_4\text{-Ag}_3\text{PO}_4$  composite, as well as metal ion concentrations, affect electron and ion motion.<sup>43</sup> Furthermore, the variations in anodic and cathodic potentials can be linked to the



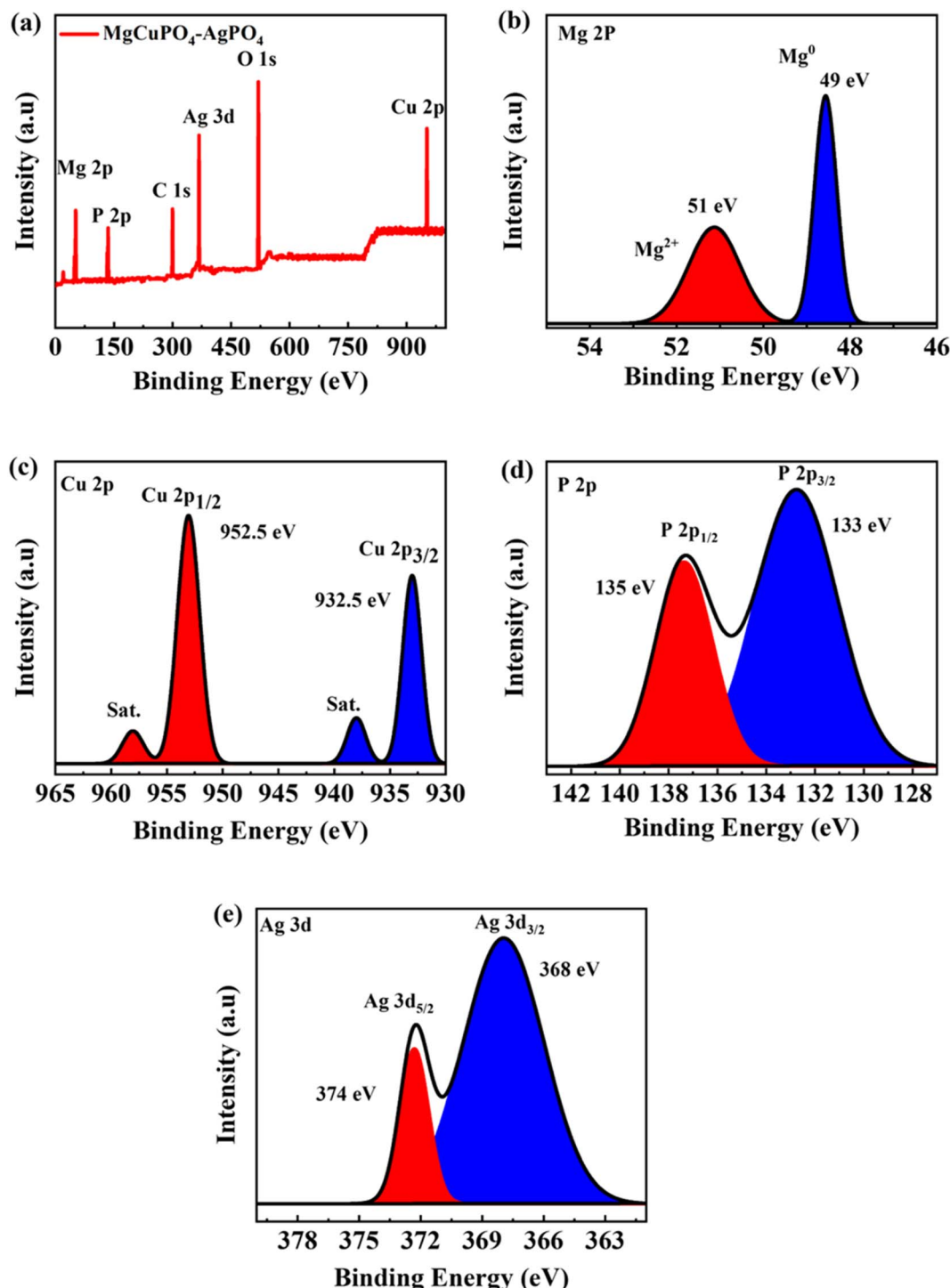


Fig. 4 (a) XPS survey spectrum for  $S_2$ . (b) XPS spectrum for Mg. (c) XPS spectrum for Cu 2p. (d) XPS spectrum for P 2p. (e) XPS spectrum for Ag 3d.

presence of the redox process.<sup>44</sup> The CV curve of  $MgCuPO_4$  changes its shape at  $100\text{ mV s}^{-1}$  (Fig. 6(a)) because the electrolyte ions did not reach the  $MgCuPO_4$  inner sites.<sup>45</sup>  $S_2$  had a greater CV area (and thus a greater specific capacity) than  $MgCuPO_4$  at a low scan rate.  $S_2$  also maintained its form at higher scan rates due to its stable behavior.<sup>46,47</sup> Fig. 6(a)–(d) illustrate the CV curves for  $S_2$  and the other samples ( $MgCuPO_4$ ,

$S_1$ , and  $S_3$ ) that were gradually enhanced with rising scan rates ( $3\text{--}50\text{ mV s}^{-1}$ ). Fig. S1† shows the CV curves for  $MgCuPO_4$ ,  $S_1$ , and  $S_3$  at an operating potential of  $0\text{--}0.8\text{ V}$ .

For battery-type materials, the most suitable word to determine the storage capability is the specific capacity ( $C\text{ g}^{-1}$ ). However, some researchers in the literature also use capacitance ( $F\text{ g}^{-1}$ ) which is not correct. Table 3 shows the values of



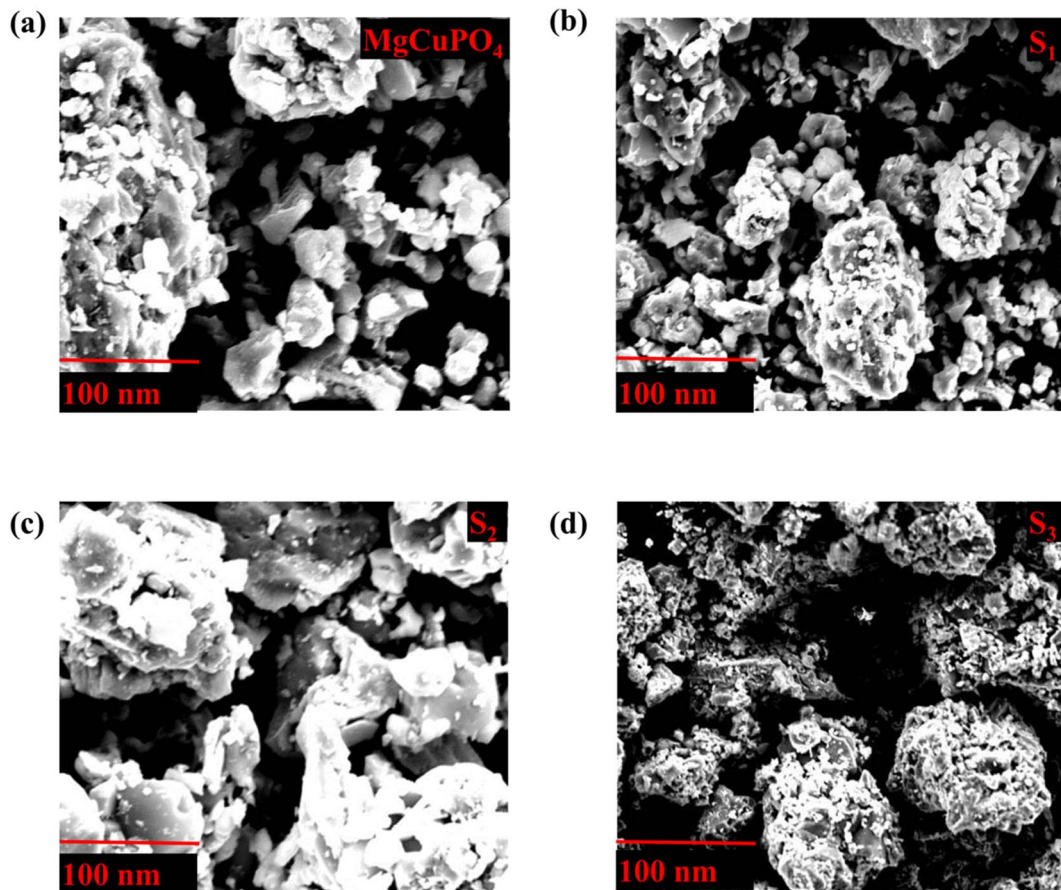


Fig. 5 (a–d) SEM images for S<sub>1</sub>, S<sub>2</sub>, S<sub>3</sub>, and S<sub>4</sub> composites.

specific capacity at all scan rates. Eqn (8) can be used to determine the specific capacity.<sup>48</sup>

$$Q_s = \frac{1}{m\Delta v} \int_{V_i}^{V_f} I \times V dV \quad (8)$$

In eqn (8),  $Q_s$  indicates the specific capacity,  $m$  is the active mass,  $\Delta v$  represents the change in scan rate; the current is denoted by  $I$ , and the operating potential by  $V$ . The specific capacities calculated for MgCuPO<sub>4</sub>, S<sub>1</sub>, S<sub>2</sub>, and S<sub>3</sub> at various scans are represented in Fig. 7(a). The specific capacities for MgCuPO<sub>4</sub>–Ag<sub>3</sub>PO<sub>4</sub> nanocomposites were higher than that for MgCuPO<sub>4</sub>. The specific capacity for S<sub>2</sub> at 3 mV s<sup>-1</sup> was 839 C g<sup>-1</sup>, which was higher than that for MgCuPO<sub>4</sub> (335 C g<sup>-1</sup>), S<sub>1</sub> (442 C g<sup>-1</sup>), or S<sub>3</sub> (671 C g<sup>-1</sup>). The specific capacities for all samples (MgCuPO<sub>4</sub>, S<sub>1</sub>, S<sub>2</sub>, and S<sub>3</sub>) at 3 mV s<sup>-1</sup> are represented in Fig. 7(b). When an amount of Ag<sub>3</sub>PO<sub>4</sub> is added into the heterostructure of MgCuPO<sub>4</sub>, the specific capacity increases due to the combined impact of MgCuPO<sub>4</sub>–Ag<sub>3</sub>PO<sub>4</sub>, with a large number of accessible pores and faster movement of ions. A further increase in the amount of Ag<sub>3</sub>PO<sub>4</sub> resulted in a decrease in its capacity. An excess amount of Ag<sub>3</sub>PO<sub>4</sub> also results in blockage of a number of pores. Therefore, the specific capacity for S<sub>3</sub> decreases.

The positive and negative current spikes measured through CV readings of S<sub>2</sub> gradually increased with the square root of the

scan rate. The value of the  $I_{pa}/I_{pc}$  fraction was almost 1. This indicated that the reversible faradaic processes were responsible for charge storage, as shown in Fig. 7(c).<sup>49</sup> The linear relation between anodic and cathodic currents was evidence of the battery nature of the MgCuPO<sub>4</sub>–Ag<sub>3</sub>PO<sub>4</sub> (S<sub>2</sub>) nanocomposite. Fig. 7(d) indicates a straight-line relationship between voltage and log of scan rate, which proves the diffusion-controlled process for S<sub>2</sub>. The chemical equations below can be used to describe redox reactions.<sup>50</sup>



The discharge profiles of MgCuPO<sub>4</sub> and MgCuPO<sub>4</sub>–Ag<sub>3</sub>PO<sub>4</sub> nanocomposites obtained using the GCD method are shown in Fig. 8(a)–(d). The shape of the GCD curves was non-linear for MgCuPO<sub>4</sub>, S<sub>1</sub>, S<sub>2</sub>, and S<sub>3</sub> because of deep ion interaction, showing that charge storage contribution comes mainly from the redox reactions. At a current density of 2 A g<sup>-1</sup>, S<sub>2</sub> had the greatest discharge time compared to the other MgCuPO<sub>4</sub>–AgPO<sub>4</sub> nanocomposite electrodes. At 3.2 A g<sup>-1</sup> current, the GCD trajectory of MgCuPO<sub>4</sub> was also relatively shorter than that of S<sub>2</sub>. This showed that the performance of MgCuPO<sub>4</sub> decreases with current density more frequently than the other MgCuPO<sub>4</sub>–



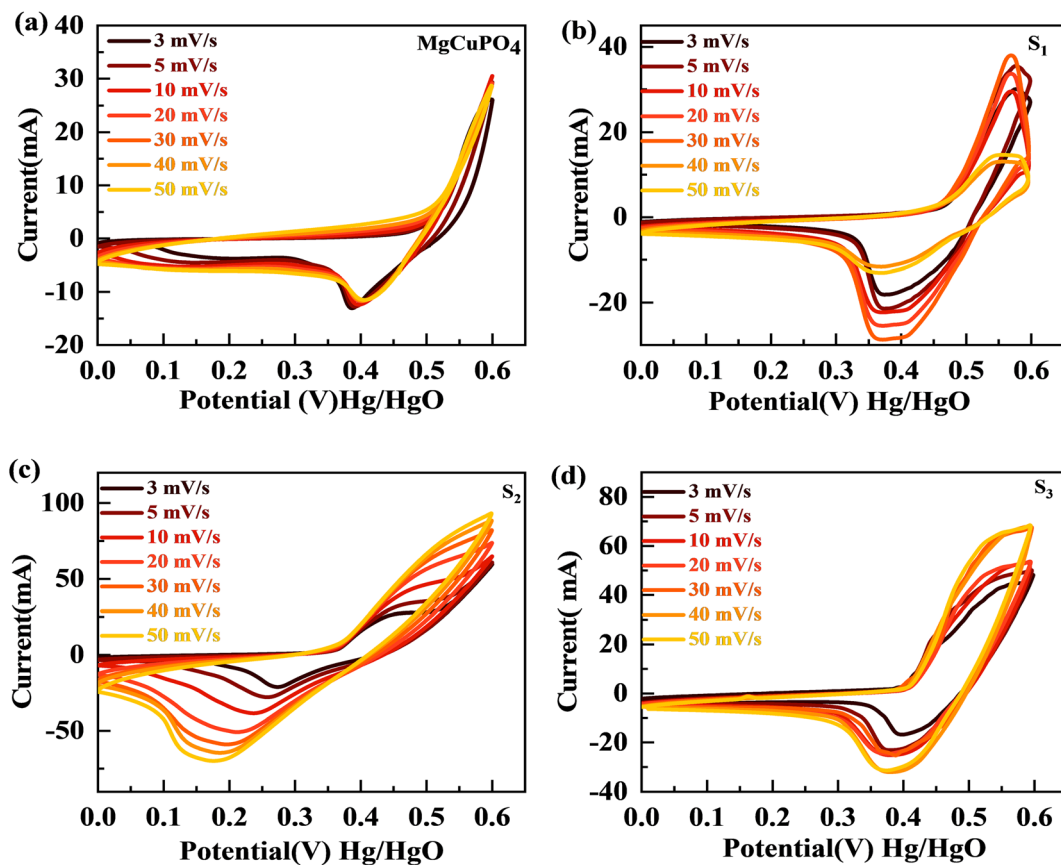


Fig. 6 (a–d) The CV curves for  $\text{MgCuPO}_4$ ,  $\text{S}_1$ ,  $\text{S}_2$ , and  $\text{S}_3$ , respectively.

$\text{Ag}_3\text{PO}_4$  nanocomposites, as illustrated by Fig. 8(a)–(d). The GCD comparison at  $2.0 \text{ A g}^{-1}$  for  $\text{MgCuPO}_4$ ,  $\text{S}_1$ ,  $\text{S}_2$ , and  $\text{S}_3$  is represented in Fig. 9(a). As can be seen from Fig. 9(a),  $\text{S}_2$  had the largest plateau region compared to the other samples. This may be due to the larger surface area exposed to electrolytic ions, faster transportation of ions, and higher conductivity of  $\text{S}_2$ . The specific capacity,  $Q_s$ , of the electrodes was determined using eqn (11) from the galvanostatic discharge data.

$$Q_s = \frac{I \times \Delta t}{m} \quad (11)$$

in eqn (11),  $Q_s$  represents the specific capacity,  $I$  is the current,  $\Delta t$  indicates the discharge time, and  $m$  is the active mass. Fig. 9(b) depicts a plot of specific capacity for  $\text{MgCuPO}_4$ ,  $\text{S}_1$ ,  $\text{S}_2$ , and  $\text{S}_3$  against current density derived from the GCD curves. At all present current densities, the specific capacity for  $\text{MgCuPO}_4$  had reduced from  $316 \text{ (2 A g}^{-1}\text{)}$  to  $169 \text{ C g}^{-1}$  ( $3.2 \text{ A g}^{-1}$ ), with 53% capacity retention.  $\text{S}_1$  had a capacity retention of 58% with a capacity of  $330 \text{ C g}^{-1}$  at  $2 \text{ A g}^{-1}$  and  $192 \text{ C g}^{-1}$  at  $3.2 \text{ A g}^{-1}$ . Again  $\text{S}_2$  outperforms the other composite materials, showing  $1138 \text{ C g}^{-1}$  capacity at  $2 \text{ A g}^{-1}$ .  $\text{S}_2$  can retain  $663.8 \text{ C g}^{-1}$  capacity at  $3.2 \text{ C g}^{-1}$  showing 59% capacity retention. Furthermore, an

Table 3 Specific capacity for  $\text{MgCuPO}_4$ ,  $\text{S}_1$ ,  $\text{S}_2$ , and  $\text{S}_3$  through CV and GCD

Scan rate ( $\text{mV s}^{-1}$ )	Specific capacity ( $\text{C g}^{-1}$ )							
	$\text{MgCuPO}_4$		$\text{S}_1$		$\text{S}_2$		$\text{S}_3$	
	CV	GCD	CV	GCD	CV	GCD	CV	GCD
3	336.16	317	442	330	839	1138	671	512
5	264.60	269	379.71	269	682.04	933	583.42	478
10	200.12	245	305.08	251	571.73	891	447.96	447
20	129.15	215	212.86	236	333.16	832	257.97	426
30	71.05	192	122.49	225	194.76	745	184.12	398
40	40.49	183	83.07	210	126.813	682	119.18	355
50	20.88285	169	49.40	192	86.44	663	70.54	313



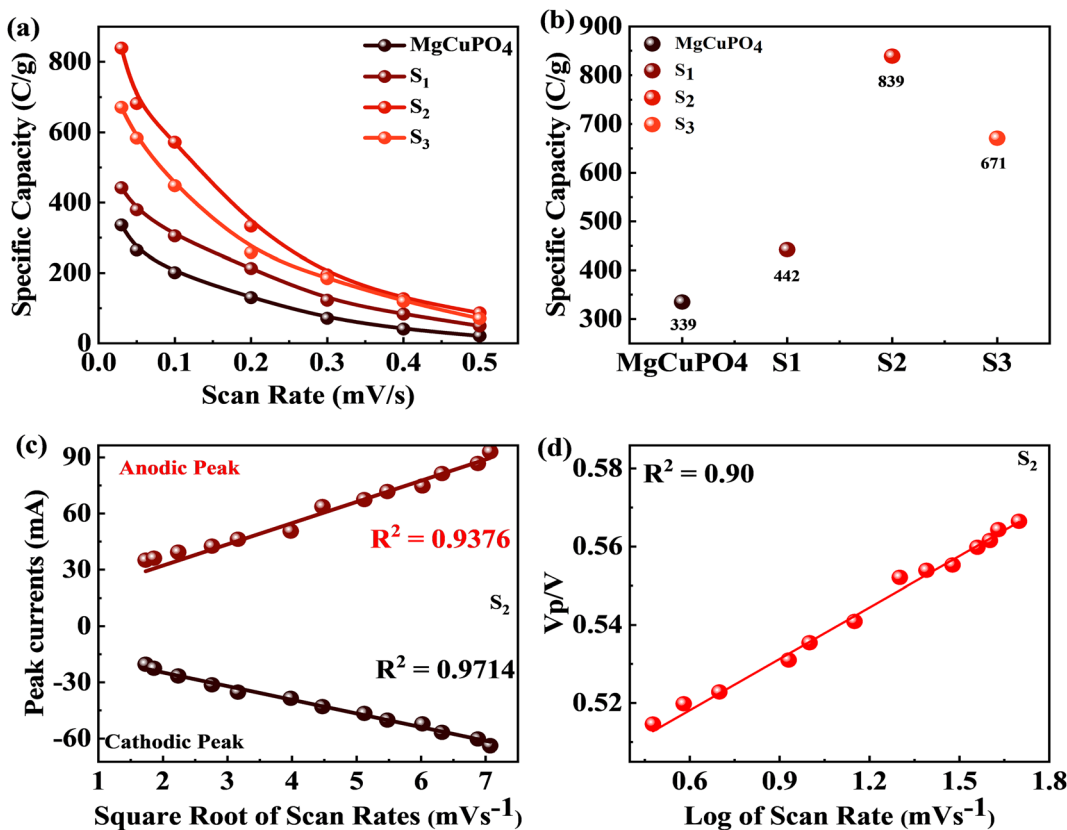


Fig. 7 (a) Specific capacity for MgCuPO<sub>4</sub>, S<sub>1</sub>, S<sub>2</sub>, and S<sub>3</sub> at various scan rates. (b) Specific capacity for MgCuPO<sub>4</sub>, S<sub>1</sub>, S<sub>2</sub>, and S<sub>3</sub> at 3 mV s<sup>-1</sup> scan rate. (c) Anodic and cathodic peaks calculated for S<sub>2</sub>. (d) Peak voltage plotted against log of scan rate for S<sub>2</sub>.

increase in the wt% ratio of Ag<sub>3</sub>PO<sub>4</sub> decreases the overall performance. The specific capacities decrease for S<sub>3</sub> to 512 C g<sup>-1</sup> at 2 A g<sup>-1</sup> and 313.6 C g<sup>-1</sup> at 3.2 A g<sup>-1</sup>, demonstrating 61% capacity retention.

This increase in rate capacity was due to the presence of Ag<sub>3</sub>PO<sub>4</sub> NPs, which decreased the internal impedance of MgCuPO<sub>4</sub>.<sup>51</sup> Among all the MgCuPO<sub>4</sub>–Ag<sub>3</sub>PO<sub>4</sub> (S<sub>1</sub>, S<sub>2</sub>, and S<sub>3</sub>) nanocomposites studied, S<sub>2</sub> had the highest capacity. The increased electrochemical performance for S<sub>2</sub> was due to two conflicting effects: raising the quantity of Ag<sub>3</sub>PO<sub>4</sub> increases the conductivity of MgCuPO<sub>4</sub>–Ag<sub>3</sub>PO<sub>4</sub> nanocomposites. However, too many Ag<sub>3</sub>PO<sub>4</sub> nanoparticles degrade the performance of the S<sub>3</sub> electrode due to agglomerations produced, which reduces the contact area between the electrode and electrolytic solution. Another cause was the lack of amorphous MgCuPO<sub>4</sub> in S<sub>3</sub>, as amorphous MgCuPO<sub>4</sub> was responsible for increased active sites for redox reactions.<sup>52</sup> Therefore, owing to the structural stability of crystalline Ag<sub>3</sub>PO<sub>4</sub> NPs, the rate capacity of S<sub>2</sub> remains greater than that of MgCuPO<sub>4</sub>. Fig. 9(c) indicates the comparative calculated specific capacities for MgCuPO<sub>4</sub>, S<sub>1</sub>, S<sub>2</sub>, and S<sub>3</sub> at 2.0 A g<sup>-1</sup>.

The electrochemical impedance spectra (EIS) of the electrode materials were measured to determine charge and ion transport. The Nyquist graphs of amorphous MgCuPO<sub>4</sub>, S<sub>1</sub>, S<sub>2</sub>, and S<sub>3</sub> are shown in Fig. 9(d). Because of the roughness of the electrode surface, uneven electric field, and varying electrochemical

activity, the form of the EIS plots departs from the semicircular shape.<sup>53</sup> The corresponding series resistance was calculated using the contact of the EIS graphs with the real part of the impedance spectrum. At high frequencies, the semicircle width is attributed to charge transfer impedance ( $R_{ct}$ ).<sup>54</sup> In Fig. 9(d) (inset), the circuit diagram for the fitted Nyquist plot is also represented. The semicircle can be seen from the ZCPE and  $R_{ct}$  parallel connection in the circuit diagram. According to the EIS diagram, the  $R_s$  values for S<sub>1</sub>, S<sub>2</sub>, S<sub>3</sub>, and MgCuPO<sub>4</sub> were 0.72, 0.65, 0.81, and 1.05 U, respectively, as shown in Fig. 9(d). The lower  $R_s$  values of all MgCuPO<sub>4</sub>–AgPO<sub>4</sub> nanocomposites compared to amorphous MgCuPO<sub>4</sub> nanocomposites suggest higher conductance. Moreover, the semicircle diameter of MgCuPO<sub>4</sub> was considerably bigger than that of the MgCuPO<sub>4</sub>–AgPO<sub>4</sub> nanocomposites in the Nyquist plots, which results in greater charge transfer resistance. In all the MgCuPO<sub>4</sub>–Ag<sub>3</sub>PO<sub>4</sub> nanocomposites studied, S<sub>2</sub> had the shortest diameter, indicating the lowest internal resistance. Furthermore, the straight line for S<sub>2</sub> was the sharpest, indicating the lowest ion diffusion resistance. The high-resolution EIS spectra for MgCuPO<sub>4</sub>, S<sub>1</sub>, S<sub>2</sub>, and S<sub>3</sub> are represented in Fig. 9(e). A potential-dependent capacity test was used to further explore the effect of Ag<sub>3</sub>PO<sub>4</sub> modification on the electrical characteristics of MgCuPO<sub>4</sub>. MS plots were made from the capacitances obtained from the imaginary portion of the impedance. Fig. 9(f) depicts the MS plots for MgCuPO<sub>4</sub>, S<sub>1</sub>, S<sub>2</sub>, and S<sub>3</sub>. The dominant charge carriers



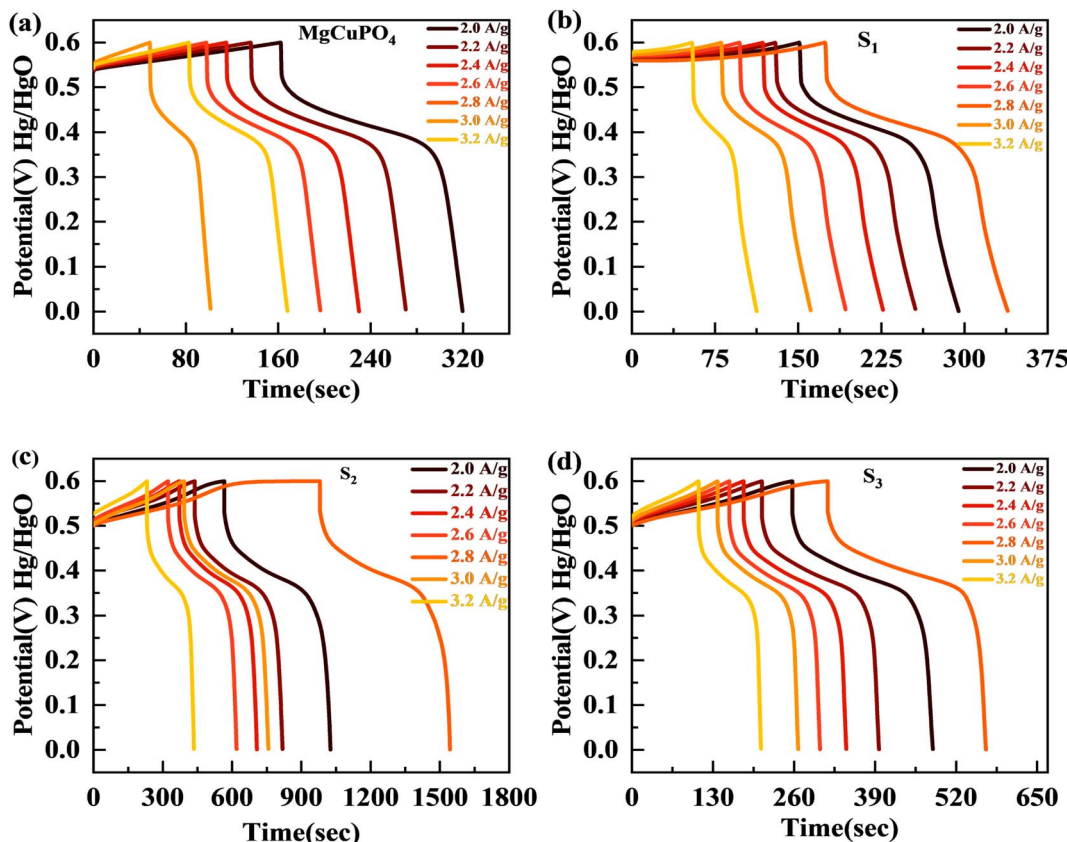


Fig. 8 (a-d) The GCD plots for  $\text{MgCuPO}_4$ ,  $\text{S}_1$ ,  $\text{S}_2$ , and  $\text{S}_3$  at different currents.

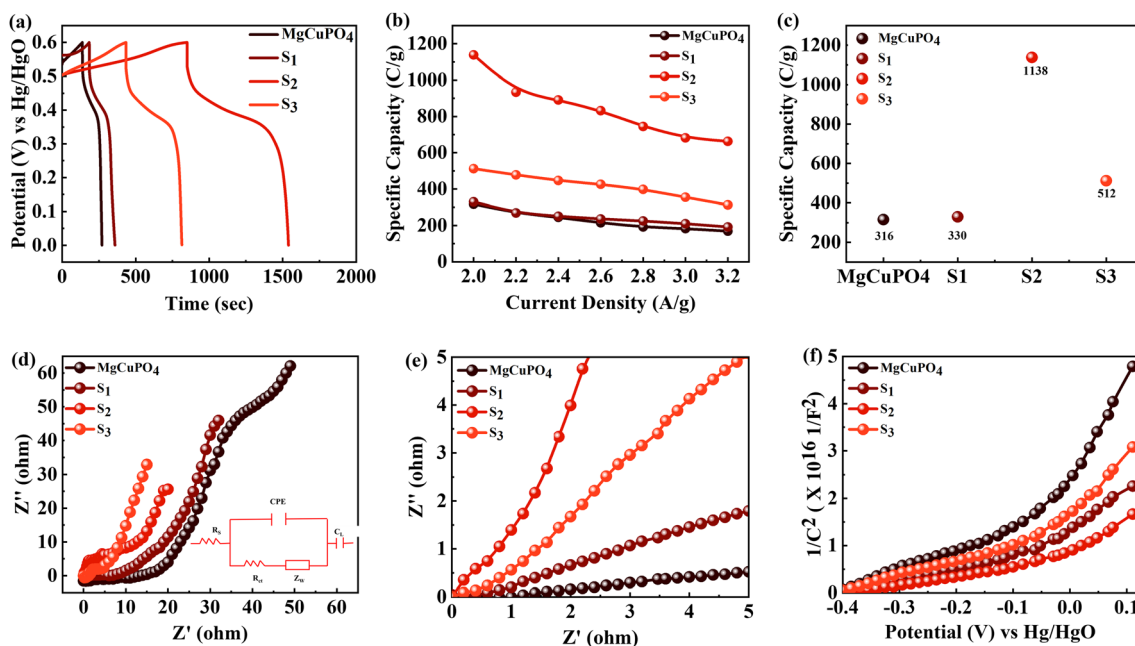


Fig. 9 (a) GCD comparison for  $\text{MgCuPO}_4$ ,  $\text{S}_1$ ,  $\text{S}_2$ , and  $\text{S}_3$  at  $2.0 \text{ A g}^{-1}$  current density. (b) Specific capacity computed for  $\text{MgCuPO}_4$ ,  $\text{S}_1$ ,  $\text{S}_2$ , and  $\text{S}_3$  at varied current densities. (c) Specific capacity computed for  $\text{MgCuPO}_4$ ,  $\text{S}_1$ ,  $\text{S}_2$ , and  $\text{S}_3$  at  $2 \text{ A g}^{-1}$  current density. (d) EIS graph for  $\text{MgCuPO}_4$ ,  $\text{S}_1$ ,  $\text{S}_2$ , and  $\text{S}_3$ . (e) High-magnification EIS images for  $\text{MgCuPO}_4$ ,  $\text{S}_1$ ,  $\text{S}_2$ , and  $\text{S}_3$ . (f) MS plot for  $\text{MgCuPO}_4$ ,  $\text{S}_1$ ,  $\text{S}_2$ , and  $\text{S}_3$ .

in all  $\text{MgCuPO}_4$ ,  $\text{S}_1$ ,  $\text{S}_2$ , and  $\text{S}_3$  materials were electrons, as indicated by the positive slope of the straight lines (n-type semiconductors). The slope obtained from the straight line plotted between  $1/C^2$  and  $V$  can be used to evaluate charge carrier density among electrode materials. The charge carrier has a negative relationship with the MS inclination.<sup>55</sup> The  $\text{S}_1$ ,  $\text{S}_2$ , and  $\text{S}_3$  slopes were lower than those of  $\text{MgCuPO}_4$ , implying that the  $\text{MgCuPO}_4\text{--Ag}_3\text{PO}_4$  composites had a greater charge carrier density. The  $\text{S}_2$  curve had the lowest slope, demonstrating its increased electron density. These findings suggest that the incorporation of  $\text{Ag}_3\text{PO}_4$  into  $\text{MgCuPO}_4$  results in a higher density of charge carriers.<sup>56</sup>

The electron transmission rate of crystalline  $\text{Ag}_3\text{PO}_4$  NPs differs from that of diffuse  $\text{MgCuPO}_4$ . The number of pores provided by  $\text{MgCuPO}_4$  was used to store the electrolyte ions that were able to penetrate the inner surface of  $\text{MgCuPO}_4$ . Most of the amorphous  $\text{MgCuPO}_4$  surfaces were engaged in the faradaic reactions. Additionally, the electrolyte could not reach internal surfaces at a higher scan rate/current density, thus producing a low specific capacity.<sup>57</sup> In contrast, the electrolytic ions interact with the topmost surface layer of  $\text{Ag}_3\text{PO}_4$  NPs as well as the inner surface of  $\text{MgCuPO}_4$ . Thus,  $\text{Ag}_3\text{PO}_4$  adds useful surface area to unutilized amorphous  $\text{MgCuPO}_4$  surfaces and maintains a large number of oxidation/reduction reactions at

higher currents.<sup>58</sup> Despite the fact that amorphous  $\text{MgCuPO}_4$  offers a porous structure that helps to store more electrolytic ions, it still had low conductance.<sup>59</sup> In this study, the high electrical conductivity of  $\text{Ag}_3\text{PO}_4$  NPs fixed on the weakly conductive amorphous  $\text{MgCuPO}_4$  accelerates the electron transfer mechanism and lowers the impedance of the  $\text{MgCuPO}_4\text{--Ag}_3\text{PO}_4$  composites. Furthermore, the  $\text{Ag}_3\text{PO}_4$  nanoparticles reduce the distance between electron transport routes and the collector, resulting in increased electrochemical performance.<sup>60</sup>

### 3.3. Supercapattery

The broad PW results in increased energy density for SCs. The supercapattery ( $\text{S}_2\text{--AC}$ ) was designed with  $\text{S}_2$  and activated carbon (AC). AC due to its permeable and porous structure allows more electrolyte ions to be stored.<sup>61</sup> The individual CV graphs were originally measured in a three-cell setup for  $\text{S}_2$  and AC to measure the overall voltage of the supercapattery (Fig. 10(a)). The working PW of AC was 0 to  $-1$  V and that of  $\text{S}_2$  was 0–0.6 V. Thus, the  $\text{S}_2\text{--AC}$  supercapattery was stable over 1.6 V. No redox peak appeared at 0–0.5 V, which showed that the dominant storage mechanism was provided by the capacitive nature of AC. At higher potential,  $>0.6$  V, redox peaks emerged, indicating the faradaic reaction of  $\text{S}_2$ . Fig. 10(b) shows that the

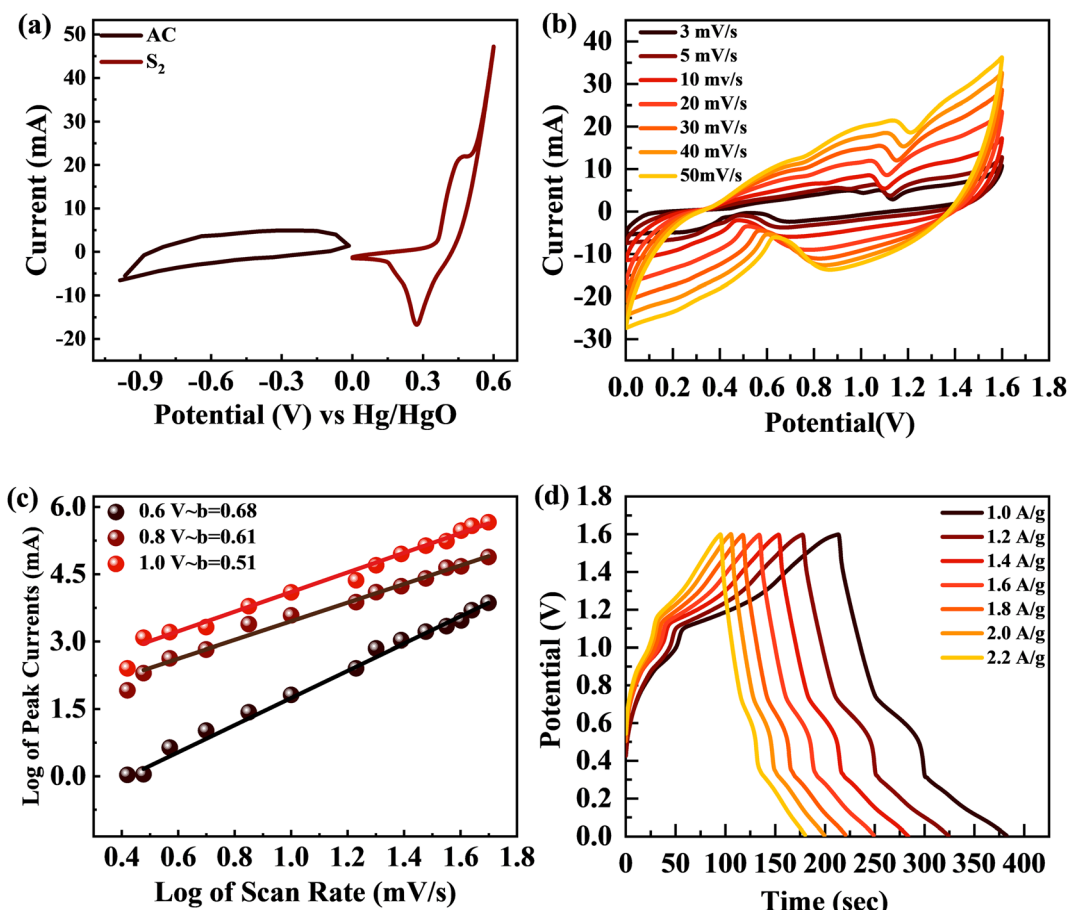


Fig. 10 (a) CV curves for AC and  $\text{S}_2$  at  $3 \text{ mV s}^{-1}$ . (b) CV curves for the  $\text{S}_2\text{--AC}$  supercapattery at  $3\text{--}50 \text{ mV s}^{-1}$ . (c)  $b$ -fitting computed for the  $\text{S}_2\text{--AC}$  device. (d) GCD curves for the  $\text{S}_2\text{--AC}$  supercapattery at  $1\text{--}2.2 \text{ A g}^{-1}$  current density.



shape of the CV graphs for the  $S_2//AC$  supercapattery was not altered at a higher scan ( $100\text{ mV s}^{-1}$ ), which proves the high stability of the  $S_2//AC$  device.

The power law, which connects current density  $I$  with scan rate ( $v$ ), was used for theoretical study of the electrochemical behavior of the asymmetric device. The charge storage process in a supercapattery is investigated using  $b$ -fitting. The  $b$ -value was calculated using the slope drawn between the log of scan rate and the log of peak current.

$$I = kv^b \quad (12)$$

$$\ln I = \ln k + b \ln v \quad (13)$$

The adjustable factors are represented by  $k$  and  $b$ , as stated in the equations, while  $v$  is the scan rate and  $I$  is the current. The exponent  $b$  is critical in deciding the charge accumulation in a supercapattery. For a  $b$ -value of 0–0.5, the dominant charge storage process is diffusion regulated. For a  $b$ -value of 0.8–1.0, the dominant charge storage process is adsorption/desorption. For a  $b$ -value of 0.5–0.8, the storage process is due to both faradaic and adsorption/desorption processes.<sup>62</sup> The  $b$ -fitting for this supercapattery ( $S_2//AC$ ) was between 0.5 and 0.8, as shown in Fig. 10(c). This proves the formation of a supercapattery.

The GCD measurements for the  $S_2//AC$  supercapattery were performed at various densities ( $1.0$  to  $2.2\text{ A g}^{-1}$ ), as depicted in Fig. 10(d). The GCD curves of the  $S_2//AC$  device were nearly symmetrical at all currents, which demonstrates its higher stability.<sup>63</sup> Furthermore, the GCD contours were non-linear due to the faradaic response of  $S_2$ . The specific capacity for the  $S_2//AC$  supercapattery was also calculated from eqn (8) and (11). At a current intensity of  $1.0\text{ A g}^{-1}$ , the specific capacity of  $S_2//AC$  was  $193\text{ C g}^{-1}$ , as indicated in Fig. 11(a). The  $S_2//AC$  device can retain 60% of its initial capacity at  $2.2\text{ A g}^{-1}$  current. While the capacity through a CV for the  $S_2//AC$  supercapattery was  $183\text{ C g}^{-1}$  (at  $3\text{ mV s}^{-1}$ ), as indicated in Fig. 11(b).

Fig. 11(c) and (d) represent the stability test for the  $S_2//AC$  supercapattery device against 5000 cycles. The capacity was increased marginally to 110% at the start, owing to the wettability of the electrode surface and slow activation of the electrode.<sup>64</sup> After 5000 cycles, the capacity declined slowly to 92%, showing that the device was stable. The coulombic efficiency after 5000 cycles was retained at 98%. The decay in capacity was due to structural degradation of the electrode materials. The nanocomposite agglomeration as well as separation of the electrode material from the electrolyte are also responsible for the decrease in capacity.<sup>65,66</sup>

Fig. 11(e) depicts the Ragone plot of the estimated energy density ( $E$ ) and power density ( $P$ ) of the  $S_2//AC$  supercapattery using the following formulae.

$$E\text{ (W h kg}^{-1}\text{)} = \frac{Q\Delta V}{2 \times 3.6} \quad (14)$$

$$P\text{ (W kg}^{-1}\text{)} = \frac{E \times 3600}{\Delta t_d} \quad (15)$$

where  $Q$  denotes specific capacity,  $V$  denotes the PW, and  $t_d$  denotes discharge duration.  $S_2//AC$  provided a high energy density as well as an outstanding power density ( $49.4\text{ W h kg}^{-1}$  at  $550\text{ W kg}^{-1}$  and  $19.5\text{ W h kg}^{-1}$  at  $6382\text{ W kg}^{-1}$ ). These results outperformed previous studies, as indicated in Table 4.

## 4. Oxygen evolution reaction (OER)

Linear sweep voltammetry (LSV) was employed to evaluate the electrocatalytic performance of  $\text{MgCuPO}_4$ ,  $S_1$ ,  $S_2$ ,  $S_3$ , and  $S_4$  composites, as well as the bare stainless steel (SS) substrate. To conduct the investigation,  $1\text{ M KOH}$  electrolyte was utilized. The primary objective was to assess their ability to generate a current density of  $10\text{ mA cm}^{-2}$  with minimal overpotential, aiming to match the widely employed anode materials  $\text{RuO}_2$  and  $\text{IrO}_2$  in various industrial applications. The LSV data revealed distinctive behavior among the tested materials.<sup>67</sup>

$$\eta = E_{\text{RHE}} - 1.23\text{ V} \quad (16)$$

The  $\text{MgCuPO}_4$  composite exhibited an onset overpotential of  $340\text{ mV}$ , whereas the  $S_1$  and  $S_3$  composites displayed starting overpotentials of  $263$  and  $221\text{ mV}$ , respectively. In contrast, the  $S_2$  composite showcased an even lower overpotential of  $142\text{ mV}$ , further underscoring its electrocatalytic capabilities. Conversely, the bare SS substrate necessitated a higher overpotential of  $388\text{ mV}$  to achieve a current density of  $10\text{ mA cm}^{-2}$  (Fig. 12(a)).

The bare SS substrate was included in the assessment as a reference point to evaluate the effectiveness of the composites. The higher overpotential required by the bare SS substrate suggests low electrocatalytic activity and inadequate efficiency in the oxygen evolution reaction (OER). Conversely, the significantly lower overpotentials observed for the  $\text{MgCuPO}_4$ ,  $S_1$ ,  $S_2$ , and  $S_3$  composites indicate superior performance and potential for diverse applications, particularly in renewable energy conversion and storage devices.

Moreover, Fig. 12(b) illustrates comparable overpotentials at  $j = 10\text{ mA cm}^{-2}$ , a typical measure of OER activity. A lower overpotential implies significantly better performance in the OER.<sup>68,69</sup> These findings highlight the exceptional electrocatalytic capabilities of the  $\text{MgCuPO}_4$ ,  $S_1$ ,  $S_2$  and  $S_3$  composites compared to the bare SS substrate. Their reduced onset overpotentials and improved catalyst utilization suggest the potential to enhance energy storage technologies and enable sustainable energy conversion processes. The effectiveness of the electrochemical processes can be improved by these materials ( $\text{MgCuPO}_4$ ,  $S_1$ ,  $S_2$ , and  $S_3$ ), taking us one step forward to a more environmentally friendly and sustainable energy density.

Tafel plots were used to analyze the reaction kinetics of the  $\text{MgCuPO}_4$ ,  $S_1$ ,  $S_2$ , and  $S_3$  materials, as shown in Fig. 12(c). The Tafel slopes reveal information about the reaction response of the materials.

$$\eta = a + b \ln i \quad (17)$$

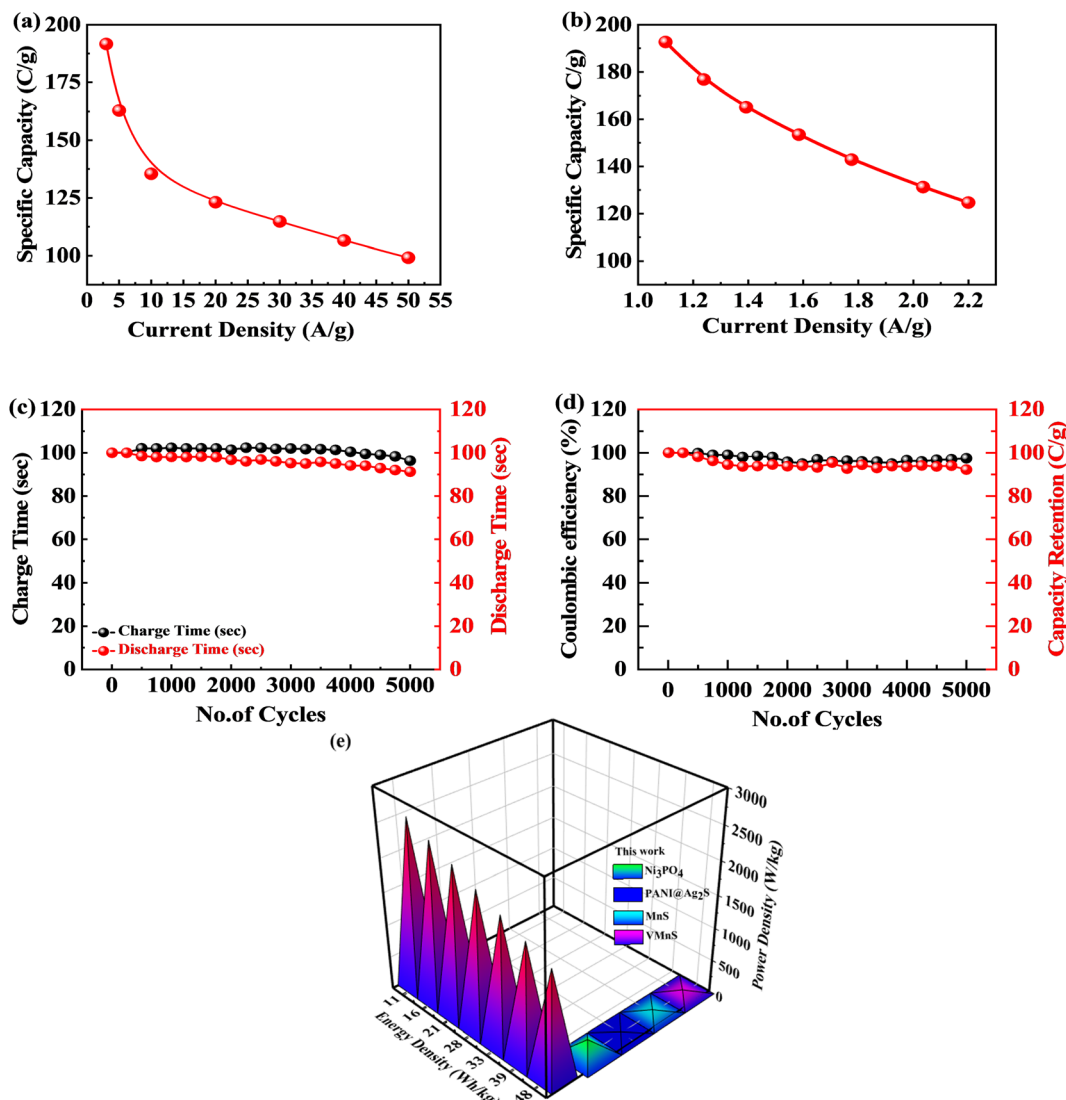


Fig. 11 (a and b) Specific capacity for the S<sub>2</sub>//AC supercapattery computed through CV and GCD. (c and d) Charge/discharge and capacity retention for the S<sub>2</sub>//AC supercapattery after 5000 cycles. (e) Energy and power density for the S<sub>2</sub>//AC supercapattery.

Table 4 Energy vs. power density for the MgCuPO<sub>4</sub>–Ag<sub>3</sub>PO<sub>4</sub>//AC device and comparison with the literature

Previous study	Energy density	Power density
Ni–Co–S <sup>70</sup>	42	750
Ni–V–S <sub>2</sub> (ref. 71)	12	900
MnS <sup>72</sup>	10.55	294.35
Sr-based materials <sup>73</sup>	21.8	224
Co/WS <sup>74</sup>	42.2	1047
2D VS <sub>2</sub> /P <sup>75</sup>	28.22	596
MnO <sub>2</sub> @CoS nanosheets <sup>76</sup>	34	597.24
<b>This work</b>	<b>49.4</b>	<b>550</b>

The MgCuPO<sub>4</sub> composite exhibits a Tafel slope of 103 mV dec<sup>-1</sup>; the S<sub>1</sub> composite shows a Tafel slope of 95 mV dec<sup>-1</sup>; S<sub>2</sub> shows a Tafel slope of 49 mV dec<sup>-1</sup> (see Table 5); and S<sub>3</sub> shows a Tafel slope of 68 mV dec<sup>-1</sup>. The reduced Tafel slope of S<sub>2</sub>

(117 mV dec<sup>-1</sup>) in comparison to the other composites and bare SS points to quicker reaction rates. As a result, the oxygen evolution process (OER) can occur at greater speeds in the S<sub>2</sub> composite due to its more effective catalytic activity.

The charge transport process inside the MgCuPO<sub>4</sub>, S<sub>1</sub>, S<sub>2</sub>, and S<sub>3</sub> materials, along with the bare SS substrate, was examined using electrochemical impedance spectra (EIS), in conjunction with Tafel studies. Significant features were discovered from the Nyquist plots, as illustrated in Fig. 12(d). Surprisingly, the semicircle diameter of the S<sub>2</sub> composite was less than those of the MgCuPO<sub>4</sub>, S<sub>1</sub>, S<sub>2</sub>, and S<sub>3</sub> composites. This suggests that the S<sub>2</sub> composite is more conductive. As shown in the insets of Fig. 12(d), analogous circuits were used to analyze the EIS data. These circuits included elements that represented the impedance of the solution ( $R_s$ ), the inherent resistance ( $R_1$ ) of the catalyst, and the impedance of the electrocatalytic activity ( $R_2$ ). Notably, the electrocatalytic resistance of the S<sub>2</sub> composite



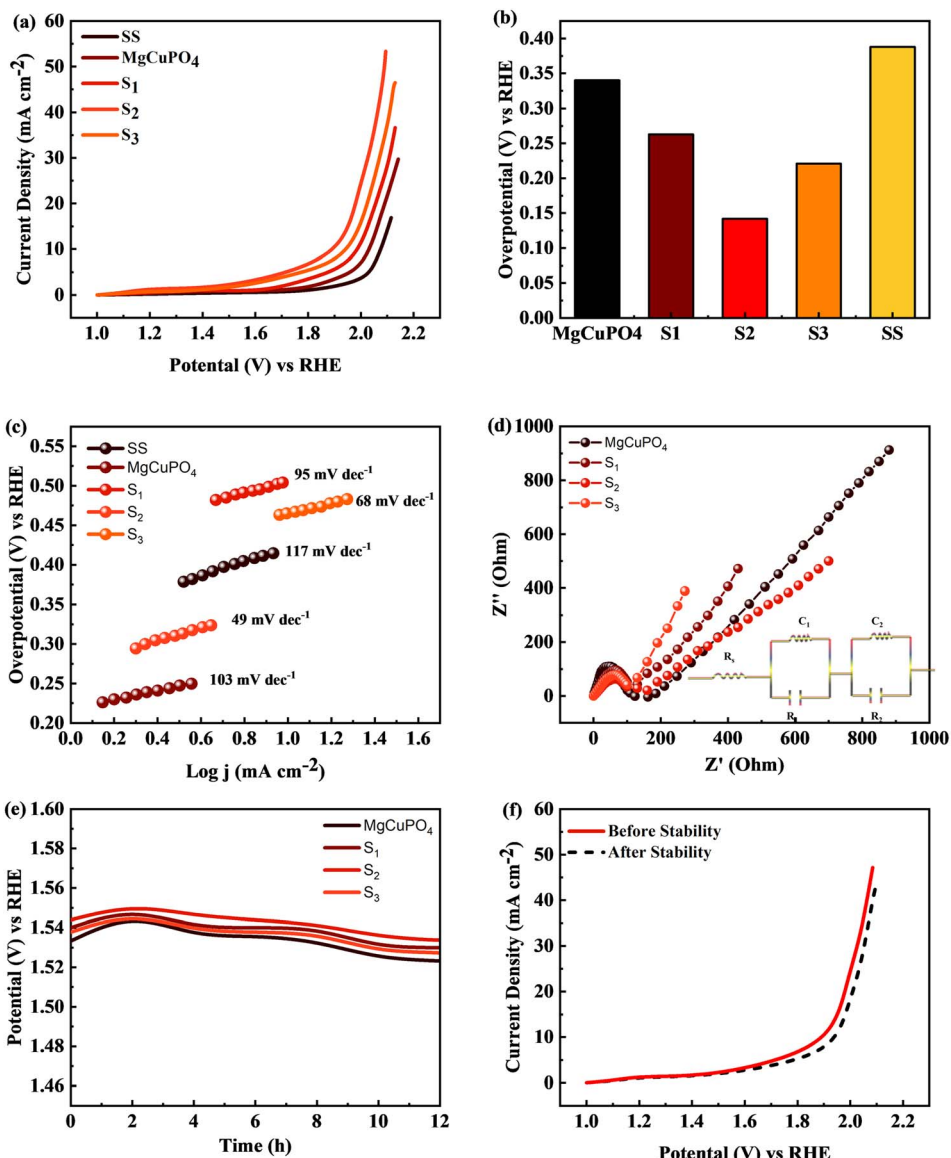


Fig. 12 (a) Linear sweep voltammograms (LSV) of MgCuPO<sub>4</sub>, S<sub>1</sub>, S<sub>2</sub>, and S<sub>3</sub> in comparison to SS. (b) Overpotential needed to achieve 10 mA cm<sup>-2</sup> current for all composites. (c) Tafel plots for SS, MgCuPO<sub>4</sub>, S<sub>1</sub>, S<sub>2</sub>, and S<sub>3</sub>. (d) EIS measurements for MgCuPO<sub>4</sub>, S<sub>1</sub>, S<sub>2</sub>, and S<sub>3</sub> composites. (e) Chronopotentiometric study for MgCuPO<sub>4</sub>, S<sub>1</sub>, S<sub>2</sub>, and S<sub>3</sub>. (f) Electrocatalytic analysis of S<sub>2</sub> composite after OER stability.

Table 5 Comparison of Tafel slope and overpotential of this work with previous studies

Literature	Tafel slope (mV dec <sup>-1</sup> )	Overpotential (mV)	Ref.
Cobalt sulfide thin films	57	300	77
Ni <sub>12</sub> P <sub>5</sub> nanocapsule	49.8	152	7
Ni <sub>x</sub> P <sub>y</sub>	72.2	157	78
C@Ni-P	64	153	79
MgCuPO <sub>4</sub> -Ag <sub>3</sub> PO <sub>4</sub> (S <sub>2</sub> )	<b>49</b>	<b>142</b>	<b>This work</b>

was determined to be 659 Ω cm<sup>2</sup>, significantly lower than the resistances of the MgCuPO<sub>4</sub> (732 Ω cm<sup>2</sup>), S<sub>1</sub> composite (788 Ω cm<sup>2</sup>) or the S<sub>3</sub> composite (914 Ω cm<sup>2</sup>). Table S1† presents the

impedance of MgCuPO<sub>4</sub>, S<sub>1</sub>, S<sub>2</sub>, and S<sub>3</sub> in the oxygen evolution reaction.

To evaluate the long-term electrochemical stability of the MgCuPO<sub>4</sub>, S<sub>1</sub>, S<sub>2</sub>, and S<sub>3</sub> composites, a chronopotentiometric mode was employed. Fig. 12(e) demonstrates a minor potential drop over time, attributed to an improvement in catalytic efficiency. Continuous gas liberation was observed during the stability investigation, indicating the ongoing oxygen evolution process. Fig. 12(f) presents the LSV graphs of S<sub>2</sub>.

The results of the study indicate that the MgCuPO<sub>4</sub>, S<sub>1</sub>, S<sub>2</sub>, and S<sub>3</sub> composites exhibit favorable reaction kinetics and long-term electrochemical stability specifically for the oxygen evolution reaction (OER). The lower Tafel slope observed for the S<sub>2</sub> composite suggests faster reaction rates, while the slight reduction in potential during the stability test signifies

improved catalytic efficiency. These characteristics are crucial for ensuring the sustained performance and durability of electrochemical devices, underscoring the significance of these composites in applications related to energy storage and conversion.

## 5. Conclusions

The sonochemical and hydrothermal technique followed by calcination treatment effectively synthesizes  $\text{MgCuPO}_4$  and  $\text{MgCuPO}_4\text{--Ag}_3\text{PO}_4$  nanocomposites with various  $\text{MgCuPO}_4\text{--Ag}_3\text{PO}_4$  content ratios. XRD phase structure analysis verified that the crystalline structure of  $\text{Ag}_3\text{PO}_4$  NPs increases with decreasing amorphous  $\text{MgCuPO}_4$  content. The FTIR spectra revealed that phosphate and hydroxyl groups were chemisorbed on the  $\text{MgCuPO}_4\text{--Ag}_3\text{PO}_4$  surface. The UV-vis spectroscopic analysis revealed that  $\text{MgCuPO}_4\text{--Ag}_3\text{PO}_4$  composites were more conductive than  $\text{MgCuPO}_4$ . The SEM analysis showed that  $\text{Ag}_3\text{PO}_4$  nanoparticles were firmly fixed on the amorphous surface of  $\text{MgCuPO}_4$ . The  $\text{MgCuPO}_4\text{--Ag}_3\text{PO}_4$  nanocomposite-based electrode demonstrated increased rate capability from 53% ( $\text{MgCuPO}_4$ ) to 59% at  $3.2 \text{ A g}^{-1}$ . The rapid electron movement and the large number of active sites given by  $\text{MgCuPO}_4$  and  $\text{Ag}_3\text{PO}_4$  composites enhanced the rate capacity. Because amorphous  $\text{MgCuPO}_4$  has a low electrical conductivity, modifying amorphous  $\text{MgCuPO}_4$  with crystalline  $\text{Ag}_3\text{PO}_4$  NPs offers a potential method to increase conductivity and rate capability. The constructed  $\text{S}_2\text{/AC}$  supercapattery had an energy density of  $49.4 \text{ W h kg}^{-1}$  at  $550 \text{ W kg}^{-1}$  power density. The  $\text{S}_2\text{/AC}$  supercapattery showed 92% capacity retention after 5000 cycles. Investigation of the OER application demonstrated that  $\text{S}_2$  exhibited the lowest Tafel slope, measuring  $49 \text{ mV dec}^{-1}$ . The results obtained from this study suggest that  $\text{MgCuPO}_4\text{--Ag}_3\text{PO}_4$  composites hold great promise as potential candidates for future energy storage devices and further investigation into the oxygen evolution reaction (OER).

## Conflicts of interest

There are no conflicts to declare.

## Acknowledgements

The authors would like to thank Princess Nourah bint Abdulrahman University Researchers Supporting Project number (PNURSP2023R9), Princess Nourah bint Abdulrahman University, Riyadh, Saudi Arabia, for supporting this project.

## References

- 1 M. F. El-Kady, M. Ihns, M. Li, J. Y. Hwang, M. F. Mousavi, L. Chaney, A. T. Lech and R. B. Kaner, *Proc. Natl. Acad. Sci. U. S. A.*, 2015, **112**, 4233–4238.
- 2 R. Kötz and M. Carlen, *Electrochim. Acta*, 2000, **45**, 2483–2498.
- 3 F. Larsson and B.-E. Mellander, *J. Electrochem. Soc.*, 2014, **161**, A1611.
- 4 F. S. Omar, A. Numan, S. Bashir, N. Duraisamy, R. Vikneswaran, Y.-L. Loo, K. Ramesh and S. Ramesh, *Electrochim. Acta*, 2018, **273**, 216–228.
- 5 G. Z. Chen, *Int. Mater. Rev.*, 2017, **62**, 173–202.
- 6 A. Numan, N. Duraisamy, F. S. Omar, D. Gopi, K. Ramesh and S. Ramesh, *Prog. Nat. Sci.: Mater. Int.*, 2017, **27**, 416–423.
- 7 H. Wan, L. Li, Y. Chen, J. Gong, M. Duan, C. Liu, J. Zhang and H. Wang, *Electrochim. Acta*, 2017, **229**, 380–386.
- 8 X. Lei, S. Ge, Y. Tan, Z. Wang, J. Li, X. Li, G. Hu, X. Zhu, M. Huang and Y. Zhu, *ACS Appl. Mater. Interfaces*, 2020, **12**, 9158–9168.
- 9 Y. Yang, Y. Zhou, Z. Hu, W. Wang, X. Zhang, L. Qiang and Q. Wang, *J. Alloys Compd.*, 2019, **772**, 683–692.
- 10 H. Moon, H. Lee, J. Kwon, Y. D. Suh, D. K. Kim, I. Ha, J. Yeo, S. Hong and S. H. Ko, *Sci. Rep.*, 2017, **7**, 41981.
- 11 L. Tang, F. Duan and M. Chen, *RSC Adv.*, 2016, **1244**, 65012–65019.
- 12 Y. Shao, H. Wang, Q. Zhang and Y. Li, *J. Mater. Chem. C*, 2013, **1**, 1245–1251.
- 13 D. S. Patil, S. A. Pawar, J. H. Kim, P. S. Patil and J. C. Shin, *Electrochim. Acta*, 2016, **213**, 680–690.
- 14 D. S. Patil, J. Shaikh, S. Pawar, R. Devan, Y. Ma, A. Moholkar, J. Kim, R. Kalubarme, C. Park and P. Patil, *Phys. Chem. Chem. Phys.*, 2012, **14**, 11886–11895.
- 15 L. Tang, F. Duan and M. Chen, *J. Mater. Sci.: Mater. Electron.*, 2017, **28**, 7769–7777.
- 16 B. Pandit, V. Devika and B. R. Sankapal, *J. Alloys Compd.*, 2017, **726**, 1295–1303.
- 17 K. M. Lee, C. W. Lai, K. S. Ngai and J. C. Juan, *Water Res.*, 2016, **88**, 428–448.
- 18 H. Hassan, M. W. Iqbal, S. Gouadria, A. M. Afzal and H. Hegazy, *J. Mater. Sci.: Mater. Electron.*, 2023, **34**, 439.
- 19 R. Mahajan, R. Prakash, S. Kumar, V. Kumar, R. Choudhary and D. Phase, *Optik*, 2021, **225**, 165717.
- 20 W. Zhao, G. Zhong, M. J. McDonald, Z. Gong, R. Liu, J. Bai, C. Yang, S. Li, W. Zhao and H. Wang, *Nano energy*, 2016, **27**, 420–429.
- 21 J.-K. Liu, C.-X. Luo, J.-D. Wang, X.-H. Yang and X.-H. Zhong, *CrysEngComm*, 2012, **14**, 8714–8721.
- 22 R. J. V. Michael, B. Sambandam, T. Muthukumar, M. J. Umapathy and P. T. Manoharan, *Phys. Chem. Chem. Phys.*, 2014, **16**, 8541–8555.
- 23 Y. Lv, H. Wang, X. Xu, J. Shi, W. Liu and X. Wang, *Chem. Eng. J.*, 2017, **326**, 401–410.
- 24 P. Benedek, N. Wenzler, M. Yarema and V. C. Wood, *RSC Adv.*, 2017, **7**, 17763–17767.
- 25 Y. Wang, K. Wang and X. Wang, *J. Colloid Interface Sci.*, 2016, **466**, 178–185.
- 26 E. Uchaker, Y. Zheng, S. Li, S. Candelaria, S. Hu and G. Cao, *J. Mater. Chem. A*, 2014, **2**, 18208–18214.
- 27 J. Zheng and C. Huang, *J. New Mater. Electrochem. Syst.*, 2002, **5**, 41–46.
- 28 V. Stefov, V. Koleva, M. Najdoski, A. Cahil and Z. Abdija, *Maced. J. Chem. Eng.*, 2020, **39**, 239–249.
- 29 Z. Hua, B. Li, L. Li, X. Yin, K. Chen and W. Wang, *J. Phys. Chem. C*, 2017, **121**, 60–69.



30 S. Saha, M. Jana, P. Khanra, P. Samanta, H. Koo, N. C. Murmu and T. Kuila, *ACS Appl. Mater. Interfaces*, 2015, **7**, 14211–14222.

31 P. Reunchan, A. Boonchun and N. Umezawa, *Phys. Chem. Chem. Phys.*, 2016, **18**, 23407–23411.

32 S. Saha, M. Jana, P. Khanra, P. Samanta, H. Koo, N. C. Murmu and T. Kuila, *RSC Adv.*, 2016, **6**, 1380–1387.

33 I. W. Hwang, C. Soci, D. Moses, Z. Zhu, D. Waller, R. Gaudiana, C. J. Brabec and A. J. Heeger, *Adv. Mater.*, 2007, **19**, 2307–2312.

34 H.-H. Huang, W.-C. Shih and C.-H. Lai, *Appl. Phys. Lett.*, 2010, **96**, 193505.

35 P. Mondal, A. Sinha, N. Salam, A. S. Roy, N. R. Jana and S. Islam, *RSC Adv.*, 2013, **3**, 5615–5623.

36 B. Wang, J. Liu, Q. Sun, R. Li, T.-K. Sham and X. Sun, *Nanotechnology*, 2014, **25**, 504007.

37 G. Yun, Q. Guan and W. Li, *RSC Adv.*, 2017, **7**, 8677–8687.

38 V. A. Kumar, T. Uchida, T. Mizuki, Y. Nakajima, Y. Katsube, T. Hanajiri and T. Maekawa, *Adv. Nat. Sci.: Nanosci. Nanotechnol.*, 2016, **7**, 015002.

39 C. A. Amarnath, N. Venkatesan, M. Doble and S. N. Sawant, *J. Mater. Chem. B*, 2014, **2**, 5012–5019.

40 S. Nagamuthu, S. Vijayakumar and K.-S. Ryu, *J. Phys. Chem. C*, 2016, **120**, 18963–18970.

41 N. Duraisamy, A. Numan, S. O. Fatin, K. Ramesh and S. Ramesh, *J. Colloid Interface Sci.*, 2016, **471**, 136–144.

42 P. Jaraba, L. Ağrı, P. Yanez-Sedeno and J. Pingarron, *Electrochim. Acta*, 1998, **43**, 3555–3565.

43 C. Chen, X. Li, F. Deng and J. Li, *RSC Adv.*, 2016, **6**, 79894–79899.

44 J. Yan, T. Wei, Z. Fan, W. Qian, M. Zhang, X. Shen and F. Wei, *J. Power Sources*, 2010, **195**, 3041–3045.

45 Z. Wu, Y. Lv, Y. Xia, P. A. Webley and D. Zhao, *J. Am. Chem. Soc.*, 2012, **134**, 2236–2245.

46 H. U. Shah, F. Wang, A. M. Toufiq, A. M. Khattak, A. Iqbal, Z. A. Ghazi, S. Ali, X. Li and Z. Wang, *Int. J. Electrochem. Sci.*, 2016, **11**, 8155–8162.

47 A. Numan, N. Duraisamy, F. S. Omar, Y. Mahipal, K. Ramesh and S. Ramesh, *RSC Adv.*, 2016, **6**, 34894–34902.

48 H. u. Hassan, M. W. Iqbal, A. M. Afzal, T. Abbas, A. Zaka, A. Yasmeen, N. A. Noor, S. Aftab and H. Ullah, *Int. J. Energy Res.*, 2022, 1–13.

49 N. Neghmouche and T. Lanez, *Int. Lett. Chem., Phys. Astron.*, 2013, **4**, 37–45.

50 H. Pang, Y.-Z. Zhang, Z. Run, W.-Y. Lai and W. Huang, *Nano Energy*, 2015, **17**, 339–347.

51 R.-Z. Li, R. Peng, K. D. Kihm, S. Bai, D. Bridges, U. Tumuluri, Z. Wu, T. Zhang, G. Compagnini and Z. Feng, *Energy Environ. Sci.*, 2016, **9**, 1458–1467.

52 L. Ma, X. Shen, Z. Ji, G. Zhu and H. Zhou, *Chem. Eng. J.*, 2014, **252**, 95–103.

53 B. Wang, X. He, H. Li, Q. Liu, J. Wang, L. Yu, H. Yan, Z. Li and P. Wang, *J. Mater. Chem. A*, 2014, **2**, 12968–12973.

54 N. Nadiah, F. S. Omar, A. Numan, Y. Mahipal, S. Ramesh and K. Ramesh, *Int. J. Hydrogen Energy*, 2017, **42**, 30683–30690.

55 Z. H. Bakr, Q. Wali, J. Ismail, N. K. Elumalai, A. Uddin and R. Jose, *Electrochim. Acta*, 2018, **263**, 524–532.

56 R. Imani, M. Pazoki, A. Tiwari, G. Boschloo, A. P. Turner, V. Kralj-Iglič and A. Iglič, *Nanoscale*, 2015, **7**, 10438–10448.

57 Z. Gao, X. Wang, J. Chang, D. Wu, L. Wang, X. Liu, F. Xu, Y. Guo and K. Jiang, *RSC Adv.*, 2015, **5**, 48665–48674.

58 S. Vadivel, D. Maruthamani, M. Kumaravel, B. Saravanakumar, B. Paul, S. S. Dhar, K. Saravanakumar and V. Muthuraj, *J. Taibah Univ. Sci.*, 2017, **11**, 661–666.

59 S. Xu, X. Li, Z. Yang, T. Wang, W. Jiang, C. Yang, S. Wang, N. Hu, H. Wei and Y. Zhang, *ACS Appl. Mater. Interfaces*, 2016, **8**, 27868–27876.

60 D. S. Patil, S. A. Pawar, R. S. Devan, M. G. Gang, Y.-R. Ma, J. H. Kim and P. S. Patil, *Electrochim. Acta*, 2013, **105**, 569–577.

61 M. S. Halper and J. C. Ellenbogen, *Supercapacitors: A Brief Overview*, The MITRE Corporation, McLean, Virginia, USA, 2006, p. 34.

62 M. Z. Iqbal, M. M. Faisal, S. R. Ali, S. Farid and A. M. Afzal, *Electrochim. Acta*, 2020, **346**, 136039.

63 Y. Ma, Y. Jia, L. Wang, M. Yang, Y. Bi and Y. Qi, *J. Mater. Chem. A*, 2016, **4**, 10414–10418.

64 G. K. Veerasubramani, K. Krishnamoorthy and S. J. Kim, *J. Power Sources*, 2016, **306**, 378–386.

65 Y. He, W. Chen, X. Li, Z. Zhang, J. Fu, C. Zhao and E. Xie, *ACS Nano*, 2013, **7**, 174–182.

66 R. Kumar, A. Agrawal, R. K. Nagarale and A. Sharma, *J. Phys. Chem. C*, 2016, **120**, 3107–3116.

67 C. Wang, A. Schechter and L. Feng, *Nano Research Energy*, 2023, **2**, e9120056.

68 J. Xu, X. Zhong, X. Wu, Y. Wang and S. Feng, *J. Energy Chem.*, 2022, **71**, 129–140.

69 K. Ham, J. Lee, K. Lee and J. Lee, *J. Energy Chem.*, 2022, **71**, 580–587.

70 J. Cao, Y. Hu, Y. Zhu, H. Cao, M. Fan, C. Huang, K. Shu, M. He and H. C. Chen, *Chem. Eng. J.*, 2021, **405**, 126928.

71 M. Z. Iqbal, M. M. Faisal, S. R. Ali and M. Alzaid, *Solid State Ionics*, 2020, **354**, 115411.

72 S. Kumar, S. Riyajuddin, M. Afshan, S. K. T. Aziz, T. Maruyama and K. Ghosh, *J. Phys. Chem. Lett.*, 2021, **12**, 6574–6581.

73 M. Z. Iqbal, A. Khan, A. Numan, S. S. Haider and J. Iqbal, *Ultrason. Sonochem.*, 2019, **59**, 104736.

74 Y. Wang and N. Herron, *J. Phys. Chem.*, 1987, **91**, 5005–5008.

75 A. Sharma, S. Kapse, A. Verma, S. Bisoyi, G. K. Pradhan, R. Thapa and C. S. Rout, *ACS Appl. Energy Mater.*, 2022, **5**, 10315–10327.

76 Q. Hu, M. Tang, M. He, N. Jiang, C. Xu, D. Lin and Q. Zheng, *J. Power Sources*, 2020, **446**, 227335.

77 S. B. Kale, A. C. Lokhande, R. B. Pujari and C. D. Lokhande, *J. Colloid Interface Sci.*, 2018, **532**, 491–499.

78 J. Li, X. Zhou, Z. Xia, W. Gao, Y. Ma and Y. Qu, *ACS Appl. Mater. Interfaces*, 2016, **8**, 10826–10834.

79 Z. Yu, L. Tetard, L. Zhai and J. Thomas, *Energy Environ. Sci.*, 2015, **8**, 702–730.

